Mode Interaction in Triple-Bay Prestressed Stayed Columns

Jialiang Yu, M. Ahmer Wadee*

Department of Civil and Environmental Engineering, Imperial College London, South Kensington Campus, London SW7 2AZ, UK

Abstract

Prestressed stayed columns are an innovative type of structural system where the compressive load-carrying capacity can be enhanced through prestressed external cable stays. A nonlinear analytical model for prestressed stayed columns with multiple crossarm systems along the column length, based on the Rayleigh–Ritz method, is presented that captures modal interactions for perfect geometries explicitly for the first time. It is demonstrated that the theoretical compressive strength enhancements under certain configurations can only be obtained at the expense of triggering a sequence of destabilizing bifurcations. This can give rise to dangerously unstable interactive post-buckling behaviour including so-called 'mode jumping' and 'snaking' phenomena. Parametric spaces where the system is most susceptible to the modal interactions are identified and it is for those configurations that the system is likely to be highly sensitive to initial imperfections. The model is validated using a nonlinear finite element model formulated within the commercial code ABAQUS and excellent comparisons are obtained.

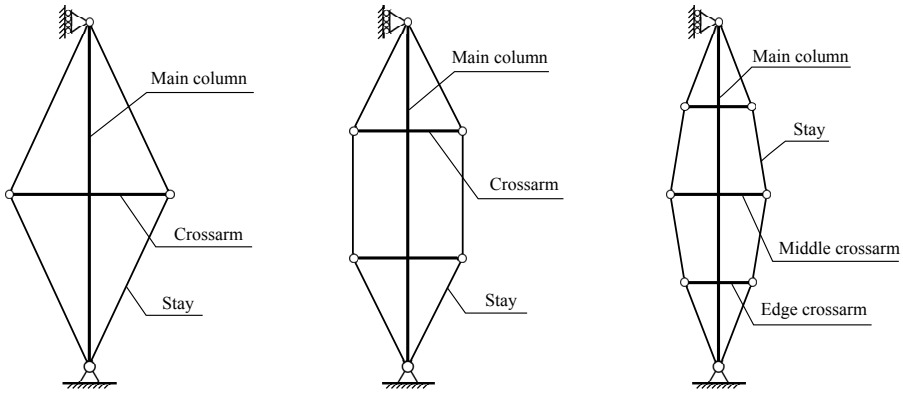
Keywords: Interactive and cellular buckling; Mode jumping; Analytical and finite element modelling; Prestressing

1. Introduction

Prestressed stayed columns, comprising a slender main column element, a system of crossarm members and pre-tensioned cable stays, as shown in Figure 1, offer an innovative, aesthetic and practical solution to the problem of low critical buckling loads in columns with highly slender geometries [1, 2, 3, 4, 5, 6, 7]. This type of element has been employed in practice where a column needs to span a long distance but has to be of relatively light-weight construction. For example, during the construction of the Rock in Rio III stadium in Brazil [8, 9], such columns were used to prop the incomplete stadium roof while the construction was completed. The columns were constructed and prestressed on site such that they eliminated the need for using expensive shoring systems that would have increased the time and cost of the construction significantly. Figure 2 shows some other

*Corresponding author

Email addresses: j.yu12@imperial.ac.uk (Jialiang Yu), a.wadee@imperial.ac.uk (M. Ahmer Wadee)



(a) Single-bay (b) Double-bay (c) Triple-bay

Figure 1: (a) The stayed column with a single crossarm system. (b)–(c) The stayed columns with multiple crossarm systems along the length. The double-bay case in (b) would be essentially identical to the particular triple-bay case shown in (c) if all the crossarms were of equal length in the latter.

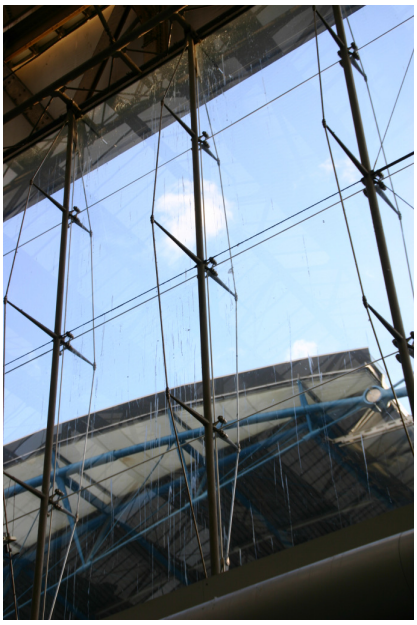
real-world applications of prestressed stayed columns.

Research on such structural components can be dated from the 1960s [10, 11, 12], although the nonlinear behaviour of prestressed stayed columns with a single crossarm system, as shown in Figure 1(a), has only been studied extensively relatively recently. This more recent work has demonstrated that although for each configuration of crossarm length, member length and stay diameter there exists a prestressing force, the so-called 'optimal prestressing force' that maximizes the critical buckling load [13], the behaviour in the post-buckling range at that level of prestress is considerably more complex [14]. Firstly, it was found that the configuration that is most sensitive to initial geometric imperfections occurs at the aforementioned optimal prestress force [15]. Secondly, it has been determined that under certain combinations the critical buckling mode switches from being symmetric to being antisymmetric about midspan. This mode switch profoundly affects the nonlinear response with modal interactions being observed numerically for configurations where the critical mode is antisymmetric [16]. This has also been found analytically from a highly simplified link model [17] and in physical experiments [18]. The work has resulted in recommendations for the level of the initial prestressing force and a detailed procedure for the design of such column systems [19, 20].

In the current work, an enhanced analytical model is presented that implements the Rayleigh–Ritz method to model the nonlinear elastic behaviour of the column as a multiple degree-of-freedom system. The bending of the main column element and the crossarms are included, as is the explicit response of the prestressed cable stays. Column arrangements with three sets of crossarms along the column span, as shown in Figure 1(c), are investigated to study the enhancement in the critical buckling load followed by the detailed post-buckling behaviour. Numerical solutions of the analytically derived equilibrium equations obtained from the continuation and bifurcation software AUTO-07P [21], demonstrate that, again, a configuration with an antisymmetric critical buckling mode is the most vulnerable to modal interactions [22, 23, 24, 25, 26] with the direct consequence of increasing the



(a) Chiswick Park, London, UK



(b) London Waterloo Station, UK



(c) Parkland Mall, Dalian, China

Figure 2: Applications of prestressed stayed columns in the construction industry; photographs (a) and (b) were taken by Daisuke Saito; photograph (c) was taken by the lead author.

sensitivity to initial imperfections. A sequence of instabilities that are intimately connected with stay slackening are found in the post-buckling range showing quantitatively, for the first time, how the post-buckling profile can be transformed from being antisymmetric to symmetric in a natural loading sequence. Moreover, the parametric ranges where the systems are most susceptible to modal interactions are identified; these configurations are best avoided in practice since they also exhibit effects synonymous with cellular buckling [27, 28, 29, 30, 31, 32], which is usually associated with dangerously unstable responses.

The analytical model is validated with a nonlinear finite element (FE) model developed within the commercial software ABAQUS [33], which has been shown in the literature to provide an excellent benchmark when compared to actual physical experiments [18]. Moreover, it has been demonstrated that for highly slender systems, elastic FE models provide an excellent prediction of the load carrying capacity [34] since the stresses within the system generally do not approach the material yield stress. The comparisons between the analytical and the FE models are shown to be excellent both qualitatively and quantitatively. This demonstrates that the analytical model captures the complex system mechanics and makes viable future parametric studies that would allow the establishment of design recommendations for stayed column systems with multiple crossarms.

2. Analytical modelling

The current investigation focuses on prestressed stayed columns with multiple bays. In the single-bay stayed column, as shown in Figure 1(a), a restraint is provided by the crossarm system at the mid-span of the column. Similarly, two restraints are provided at one-thirds and two-thirds of the column length in the double-bay case, as shown in Figure 1(b). Owing to the lack of any effective lateral stiffness at mid-span, the double-bay column cannot resist the symmetric buckling mode as effectively when compared with the triple-bay case, as shown in Figure 1(c). Results obtained as part of the current study also indicate that the load carrying capacity is much lower in the triple-bay case if the edge and the middle crossarms have the same length. This is essentially similar to the double-bay case due to the horizontal component of the stay force being zero between the two edge crossarms when the lateral displacements from global buckling are small. For the particular triple-bay case with equal length crossarms and the double-bay configuration, extra struts connecting the crossarms to the main column at midspan, in a truss-like arrangement, would potentially increase their effectiveness, but this consideration is left for future work. Therefore, the study of the triple-bay prestressed stayed column with different length crossarms is focused upon exclusively in the current work.

As shown in Figure 3, three sets of crossarms are rigidly connected to the one-quarter,

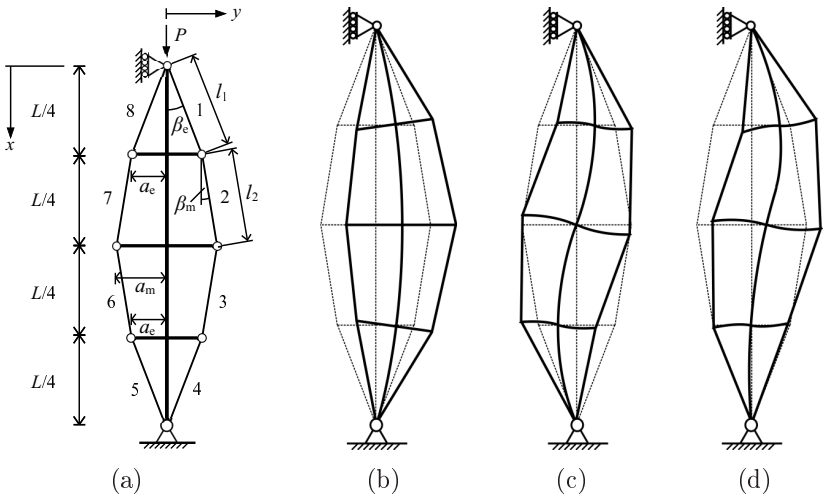
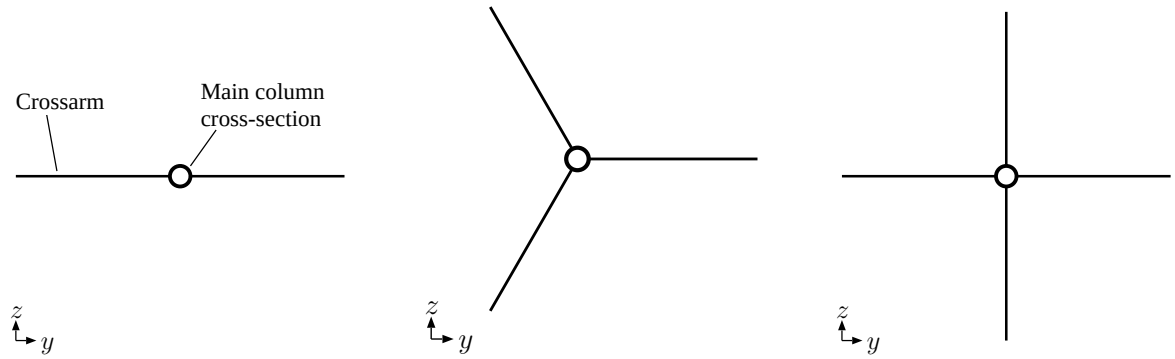


Figure 3: (a) The triple-bay prestressed stayed column with geometric and stay number definitions (1–8 inclusive); (b) symmetric buckling Mode 1; (c) antisymmetric buckling Mode 2; (d) interactive post-buckling profile.

one-half and three-quarter length points of the simply supported column. Prestressed cable stays are assumed to be pinned to the ends of the column and the tips of the crossarms. The length ratio of the edge to the middle crossarms, $\gamma = a_e/a_m$, is set to be between 0.5 and 1.0, otherwise at least one of the crossarms would initially be in tension and potentially lose effectiveness as buckling restraints since the welded connections between the main column and the crossarms may become vulnerable to fracture.

Different arrangements of crossarms along the length in the yz-plane may be used, as shown in Figure 4 with (a) showing the simplest one-dimensional system with both (b)



(a) 2 branches (b) 3 branches (c) 4 branches

Figure 4: Different numbers of branches in each crossarm system along the length. Case (a) is only practical if the buckling displacements are constrained to be purely in the y-direction; cases (b) and (c) would work if the column displaces anywhere in the yz-plane.

and (c) showing two-dimensional systems. Note that the column in practice should be supported by at least three crossarms in the yz-plane. This would ensure that it would benefit from the increased load carrying capacity by avoiding an obviously weaker buckling axis, assuming that the main column element is either a circular or square hollow section. The single-bay case with a three crossarm rosette was studied recently in [35] and as a potential unit cell in a lattice material [36]. Currently, the triple-bay system is assumed to have either the case shown in Figure 4(a) with deflections in the z-direction completely restrained or, effectively, the case shown in Figure 4(c) where it has been demonstrated previously that the system has no preferred buckling direction [15]. These two respective cases are also represented in the photographs shown in Figures 2(b) and 2(c) respectively. Hence, a two-dimensional model in the xy-plane, as depicted in Figure 3(a), is studied currently since it is simple yet practical.

Shape functions of the column and the crossarms are introduced such that the Rayleigh–Ritz method may be implemented to find the equilibrium equations from minimizing the total potential energy. The total potential energy V is obtained by summing the strain energy stored in the entire system minus the work done by the external load. The resulting nonlinear equilibrium equations can then be solved in the continuation and bifurcation software AUTO-07P [21] to reveal the critical and post-buckling behaviour of the column. Moreover, the bifurcational structure of the mechanical system is maintained which provides key information regarding modal interactions and any potential sensitivities to initial geometric imperfections.

2.1. Benchmark prestressing force

An initial prestressing force is applied to the cable stays in order to increase the load carrying capacity. The left-hand graph presented in Figure 5 depicts the relationship

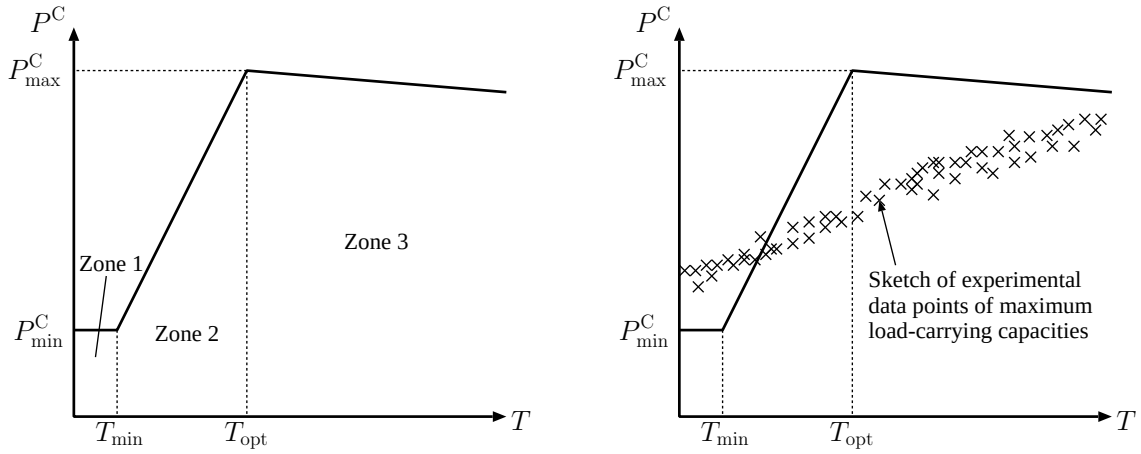


Figure 5: Critical buckling load P^{C} versus initial prestressing force T with (left) the zone distinction determined by Hafez *et al* [13] and (right) the actual ultimate strengths of stayed columns from experiments superimposed on the same graph determined by Temple [37].

between the critical buckling load and different levels of prestressing force that has been found in previous work [13]. Zone 1 represents a very small prestressing force, $T < T_{\mathrm{min}}$, which vanishes before or precisely when the critical buckling load of the main column element is reached ($P^{\mathrm{C}}_{\mathrm{min}}$) while applying the axial external load. Zone 2 represents a larger prestressing force, $T = [T_{\mathrm{min}}, T_{\mathrm{opt}}]$, which increases the load capacity of the column to be larger than the critical buckling load of the unstayed main column element. However, the stay strains vanish precisely when buckling is triggered. Zone 3 represents an even larger prestressing force such that there are residual tensile forces in the stays when buckling is triggered. The prestressing force T_{opt}, at the boundary of Zones 2 and 3, has been historically termed the 'optimal prestressing force', since it represents the prestressing force that maximizes the critical buckling load ($P^{\mathrm{C}}_{\mathrm{max}}$). The expression for the optimal prestressing force for the single-bay stayed column was presented by Hafez *et al* [13]. By a similar, but slightly extended, calculation for the triple-bay stayed column, an expression for the optimal prestressing force T_{opt} can be expressed thus:

$$T_{\mathrm{opt}} = P^{\mathrm{C}} \frac{C_{11}}{C_{22}}, \tag{1}$$

where:

$$\begin{aligned} C_{11} &= \frac{\cos\beta_{\mathrm{m}}}{2K_{\mathrm{c}}\left[\dfrac{2}{K_{\mathrm{s2}}} + \dfrac{\cos^2\beta_{\mathrm{m}}}{K_{\mathrm{c}}} + \dfrac{4\sin^2\beta_{\mathrm{m}} + 2\gamma(\sin\beta_{\mathrm{e}}\sin\beta_{\mathrm{m}} - \sin^2\beta_{\mathrm{m}})}{K_{\mathrm{m}}}\right]}, \\ C_{22} &= 1 + \frac{\cos\beta_{\mathrm{e}}\cos\beta_{\mathrm{m}}}{2K_{\mathrm{c}}\left[\dfrac{1}{K_{\mathrm{s2}}} + \dfrac{2\sin^2\beta_{\mathrm{m}} + \gamma(\sin\beta_{\mathrm{e}}\sin\beta_{\mathrm{m}} - \sin^2\beta_{\mathrm{m}})}{K_{\mathrm{m}}}\right]}, \end{aligned} \tag{2}$$

with $\gamma = a_{\mathrm{e}}/a_{\mathrm{m}}$ and:

$$\beta_{\mathrm{e}} = \arctan(4\alpha_{\mathrm{e}}), \quad \beta_{\mathrm{m}} = \arctan\left[4(\alpha_{\mathrm{m}} - \alpha_{\mathrm{e}})\right], \tag{3}$$

where $\alpha_{\mathrm{e}} = a_{\mathrm{e}}/L$ and $\alpha_{\mathrm{m}} = a_{\mathrm{m}}/L$ with K_{c}, K_{m} and K_{s2} being the axial stiffness of the main column, the middle crossarm and stay number 2:

$$K_{\mathrm{c}} = \frac{E_{\mathrm{c}}A_{\mathrm{c}}}{L}, \quad K_{\mathrm{m}} = \frac{E_{\mathrm{a}}A_{\mathrm{a}}}{a_{\mathrm{m}}}, \quad K_{\mathrm{s2}} = \frac{E_{\mathrm{s}}A_{\mathrm{s}}}{l_2}, \tag{4}$$

where E_{c}, E_{a} and E_{s} are the Young's Moduli with A_{c}, A_{a} and A_{s} being the cross-sectional areas of the main column, the crossarm and the stays respectively. The length of stay 2, l_2, is $L\sqrt{(\alpha_{\mathrm{m}} - \alpha_{\mathrm{e}})^2 + 1/16}$. The critical buckling load P^{C} is evaluated from linear eigenvalue analysis of the stayed column system by the commercial FE package ABAQUS [33] without the consideration of the prestressing force, a procedure that has been successfully applied previously [16]. Note that the optimal prestressing force T_{opt} is used as a benchmark in the current study since it is derived from a purely elastic model that does not take any geometrically nonlinear behaviour into account. It has been found previously [37] that the ultimate response of the stayed column system is more complex and that the actual failure loads of such systems are in fact maximized at initial prestressing levels that are above and beyond $T = T_{\mathrm{opt}}$, as represented in the right-hand graph of Figure 5. In fact, a relatively recent study was presented in [19] to determine the actual optimal prestressing force for the single-bay column case. This was presented primarily in terms of the maximizing the actual load carrying capacity for geometrically imperfect stayed columns; it was indeed confirmed that the initial prestressing force should be considerably larger than the value obtained by linear analysis ($T = T_{\mathrm{opt}}$). In the current study, therefore, the cases where $T \geqslant T_{\mathrm{opt}}$ are focused upon exclusively; this in fact allows the analytical model to be simplified, the precise details of which are discussed later.

2.2. Shape function of the main column

The buckling profile of the main column element can be expressed as a combination of a symmetric shape W_1 (Mode 1) and an antisymmetric shape W_2 (Mode 2) thus:

$$W_1(x) = \sum_{i=1}^{n} Q_{2i-1} L \sin\left[\frac{(2i-1)\pi x}{L}\right], \quad W_2(x) = \sum_{i=1}^{n} Q_{2i} L \sin\left(\frac{2i\pi x}{L}\right), \tag{5}$$

where Q_j is the generalized coordinate for the buckling mode shape contribution that contains j half-sine waves with L being the total length of the main column. The adoption of a larger j value allows the expressions above to describe more sophisticated and hence more accurate deformation profiles, but of course results in more equations to be solved, thereby increasing the complexity of the model. The generalized shape of the column may be obtained by combining the two distinct buckling shapes that would break both the reflective and rotational symmetries if modal interactions are triggered, as shown in Figure 3(d):

$$W(x) = W_1(x) + W_2(x) = \sum_{i=1}^{2n} Q_i L \sin\frac{i\pi x}{L}. \tag{6}$$

The normalized horizontal deflections of the main column element δ_1, δ_2 and δ_3 at the one-quarter, one-half and three-quarter length points respectively can be expressed as thus:

$$\delta_1 L = W(L/4), \quad \delta_2 L = W(L/2), \quad \delta_3 L = W(3L/4). \tag{7}$$

Ideally, the rotation of the column about the vertical axis θ_1, θ_2 and θ_3 at the one-quarter, one-half and three-quarter length points can be expressed to leading order as:

$$\theta_1 = -W'(L/4), \quad \theta_2 = -W'(L/2), \quad \theta_3 = -W'(3L/4), \tag{8}$$

where primes denote differentiation with respect to x. However, owing to the restraints provided by the crossarms, the actual rotations transferred to the crossarms may be expected to be different from those obtained using the expressions in Eq. (8). Therefore the relationship between the main column and the crossarm rotations is expressed by introducing a calibration factor κ:

$$\theta_{ai} = \kappa \theta_i, \tag{9}$$

where $i = \{1, 2, 3\}$ and the value of κ is evaluated with assistance from the FE model presented later.

2.3. Shape functions of the crossarms

There are three sets of crossarms in the triple-bay prestressed stayed column. Firstly, since a lateral point load is applied to each crossarm from the stays, a cubic shape function $W_{\mathrm{R1}}(y)$ is assumed to describe the top right crossarm, thus:

$$W_{\mathrm{R1}}(y) = C_0 + C_1 y + C_2 y^2 + C_3 y^3, \tag{10}$$

as shown in Figure 6. Four boundary conditions need to be evaluated for this crossarm:

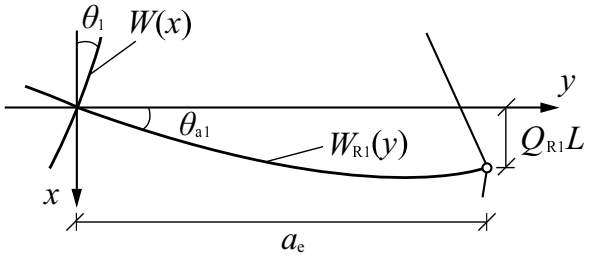


Figure 6: The deflected shape of the top right crossarm.

(1) the deflection at the left-hand end of the crossarm is zero, hence $W_{\mathrm{R1}}(0) = 0$; (2) the deflection at the right-hand end of the crossarm is defined as $Q_{\mathrm{R1}}L$, hence $W_{\mathrm{R1}}(a_{\mathrm{e}}) = Q_{\mathrm{R1}}L$ with Q_{R1} being a new generalized coordinate; (3) the left-hand side of the crossarm is rigidly connected to the main column, therefore the rotation of the crossarm at the connection is related to the rotation of the main column at the one-quarter length, hence $\dot{W}_{\mathrm{R1}}(0) = \theta_{\mathrm{a1}}$ as discussed above; (4) the right-hand end of the crossarm is pinned to the stays, therefore

there is no bending moment at the end, hence $\ddot{W}_{\mathrm{R}1}(a_{\mathrm{e}}) = 0$. Note that dots represent differentiation with respect to y and that the compression in the crossarm from the stay is neglected. The latter assumption simplifies the analysis since iteration is not required to determine the shape function of the crossarm; this marks a departure from earlier work [14]. The shape function of the top right-hand crossarm $W_{\mathrm{R}1}(y)$ can be obtained by solving for the constants C_0, C_1, C_2 and C_3 using the aforementioned boundary conditions. The shape functions of the other five crossarms can also be obtained by assuming similar cubic functions and boundary conditions with new generalized coordinates $Q_{\mathrm{R}i}$ and $Q_{\mathrm{L}i}$; the detailed expressions for all the crossarms are thus:

$$\begin{aligned} W_{\mathrm{R}i}(y) &= \kappa\theta_i y - \frac{(a_i\kappa\theta_i - Q_{\mathrm{R}i}L)\,(3a_i - y)\,y^2}{2a_i^3}, \\ W_{\mathrm{L}i}(y) &= \kappa\theta_i y - \frac{(a_i\kappa\theta_i - Q_{\mathrm{L}i}L)\,(3a_i - y)\,y^2}{2a_i^3}, \end{aligned} \tag{11}$$

where $i = \{1, 2, 3\}$ with $a_1 = a_3 = a_{\mathrm{e}}$ and $a_2 = a_{\mathrm{m}}$. Note that in the pure symmetric buckling case (Mode 1): $|W_{\mathrm{R}1}(y)| = |W_{\mathrm{R}3}(y)|$ and $|W_{\mathrm{L}1}(y)| = |W_{\mathrm{L}3}(y)|$, while $W_{\mathrm{R}2}(y) = W_{\mathrm{L}2}(y) = 0$ because the crossarms at the middle section do not bend. Similarly in the pure antisymmetric buckling case (Mode 2): $|W_{\mathrm{R}1}(y)| = |W_{\mathrm{L}3}(y)|$, $|Q_{\mathrm{L}1}| = |Q_{\mathrm{R}3}|$ and $|W_{\mathrm{R}2}(y)| = |W_{\mathrm{L}2}(y)|$. However, since the general column shape function in this study is capable of describing an asymmetric buckling shape, which is a key nonlinear deformation profile describing interactive buckling, the shape functions of the three sets of crossarms could all in fact be different to each other; this is of course allowable within the current model framework.

2.4. Strain energy stored within the stays

Figure 7 shows the generalized deformed shape of the column. The strains in each stay can be determined, which in turn allows the evaluation of the axial strain energy stored within them. Before applying any prestressing force and external load, the original lengths of stays 1, 4, 5 and 8 are:

$$l_1 = l_4 = l_5 = l_8 = L\sqrt{\alpha_{\mathrm{e}}^2 + 1/16}, \tag{12}$$

while the original lengths of stays 2, 3, 6 and 7 are:

$$l_2 = l_3 = l_6 = l_7 = L\sqrt{(\alpha_{\mathrm{m}} - \alpha_{\mathrm{e}})^2 + 1/16}, \tag{13}$$

with the stay numbering system being defined in Figure 3(a). As the external load P is introduced, the column would compress purely and this is denoted by the generalized coordinate δ_c. Since the column is assumed to be very slender, δ_c is assumed to be sufficiently small to have no significant effect on the stay lengths, but it does facilitate the definition of the pre-buckling equilibrium path. When the main column begins to deflect laterally by $W(x)$, however, the stays would be affected significantly and an additional variable Δ is

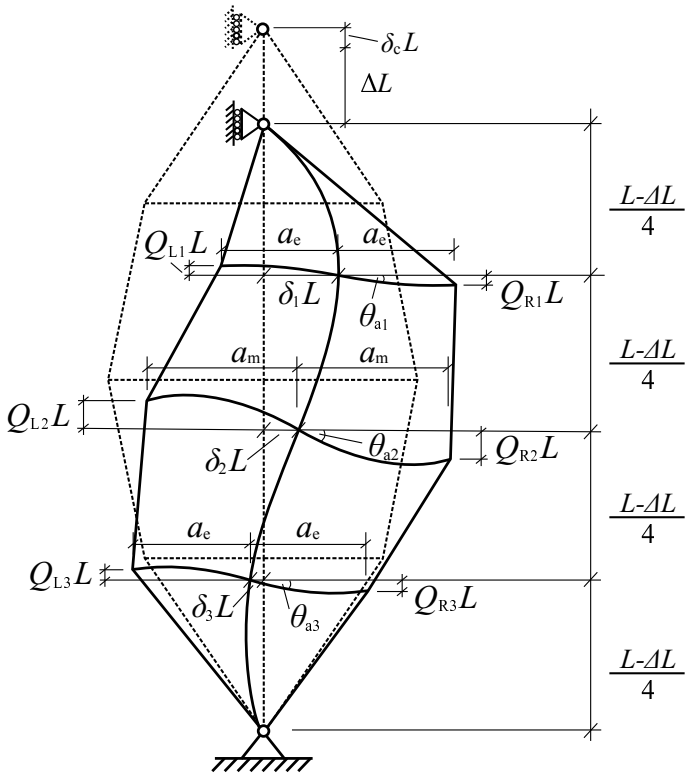


Figure 7: The generalized deflected shape of the prestressed stayed column with the defined variables.

introduced that is dependent on the deflected shape and is therefore purely a function of Q_i. Hence, the expressions for the new lengths of each stay l'_i are:

$$
\begin{aligned}
l'_1 &= L\sqrt{(\Lambda + Q_{\mathrm{R1}})^2 + (\alpha_\mathrm{e} + \delta_1)^2}, \\
l'_2 &= L\sqrt{(\Lambda - Q_{\mathrm{R1}} + Q_{\mathrm{R2}})^2 + \big[\,(\alpha_\mathrm{m} + \delta_2) - (\alpha_\mathrm{e} + \delta_1)\,\big]^2}, \\
l'_3 &= L\sqrt{(\Lambda - Q_{\mathrm{R2}} + Q_{\mathrm{R3}})^2 + \big[\,(\alpha_\mathrm{m} + \delta_2) - (\alpha_\mathrm{e} + \delta_3)\,\big]^2}, \\
l'_4 &= L\sqrt{(\Lambda - Q_{\mathrm{R3}})^2 + (\alpha_\mathrm{e} + \delta_3)^2}, \\
l'_5 &= L\sqrt{(\Lambda + Q_{\mathrm{L3}})^2 + (\alpha_\mathrm{e} - \delta_3)^2}, \\
l'_6 &= L\sqrt{(\Lambda - Q_{\mathrm{L3}} + Q_{\mathrm{L2}})^2 + \big[\,(\alpha_\mathrm{m} - \delta_2) - (\alpha_\mathrm{e} - \delta_3)\,\big]^2}, \\
l'_7 &= L\sqrt{(\Lambda - Q_{\mathrm{L2}} + Q_{\mathrm{L1}})^2 + \big[\,(\alpha_\mathrm{m} - \delta_2) - (\alpha_\mathrm{e} - \delta_1)\,\big]^2}, \\
l'_8 &= L\sqrt{(\Lambda - Q_{\mathrm{L1}})^2 + (\alpha_\mathrm{e} - \delta_1)^2},
\end{aligned}
\tag{14}
$$

where $\Lambda = (1 - \Delta)/4$. Apart from the strains generated by changing the stay lengths, there is also a pre-existing strain introduced by the initial prestressing force that can be

expressed thus:

$$\epsilon_T = \frac{T}{E_\mathrm{s} A_\mathrm{s}}, \tag{15}$$

where T is the initial prestressing force applied in the stay. Therefore, the total strain in each stay can be expressed as:

$$\epsilon_i = l_i'/l_i + \epsilon_\mathrm{T} - 1, \tag{16}$$

where i represents the stay number, as shown in Figure 3(a), and ranges from 1 to 8. Of course the expression implies that tensile strain is assumed to be positive. The strain energy of a single stay can then be expressed thus:

$$U_{\mathrm{s}i} = \frac{1}{2} E_\mathrm{s} A_\mathrm{s} l_i \epsilon_i^2, \tag{17}$$

so long as the strain ϵ_i remains positive. It can be observed that when the column begins to deflect laterally, the strain energy within the stays on the convex side would increase as the magnitude of the bending curvature in the main column element becomes larger, while the strain energy within the stays on the concave side would decrease commensurately. Eventually, one or more stays on the concave side of the column go slack when the column end displacement reaches certain values. Since the stays cannot resist compression or bending it implies that components of the strain energy should effectively vanish when the stay strains decrease to zero and below. To model this discontinuous behaviour in terms of the strain energy, a series of switches S_i are introduced into the energy formulation, hence:

$$U_\mathrm{s} = \frac{1}{2} E_\mathrm{s} A_\mathrm{s} \sum_{i=1}^{8} S_i l_i \epsilon_i^2, \tag{18}$$

where:

$$S_i = \begin{cases} 1 & \epsilon_i \geqslant 0, \\ 0 & \epsilon_i < 0. \end{cases} \tag{19}$$

Note that during the interactive buckling process, the stays on the concave side may become slack at various different times owing to the broken symmetry introduced as the symmetric Mode 1 and the antisymmetric Mode 2 couple nonlinearly.

2.5. Strain energy from bending

Strain energy from bending exists in the column and the crossarm elements. With the introduction of the respective shape functions, the bending energy of the main column U_cb is obtained by the expression:

$$U_\mathrm{cb} = \frac{1}{2} E_\mathrm{c} I_\mathrm{c} \int_0^L W''^2 \, \mathrm{d}x, \tag{20}$$

where I_c is the second moment of area of the main column element. The bending energy stored in the three sets of crossarms on the right-hand side and the left-hand side of the

main column are obtained from the respective expressions:

$$U_{\mathrm{R}i} = \frac{1}{2} E_{\mathrm{a}} I_{\mathrm{a}} \int_0^{a_i} \ddot{W}_{\mathrm{R}i}^2 \, \mathrm{d}y, \quad U_{\mathrm{L}i} = \frac{1}{2} E_{\mathrm{a}} I_{\mathrm{a}} \int_0^{a_i} \ddot{W}_{\mathrm{L}i}^2 \, \mathrm{d}y, \tag{21}$$

where I_{a} is the second moment of area of each crossarm element, which are all assumed to have the same value currently. In these two expressions $i = \{1, 2, 3\}$ with $a_1 = a_3 = a_{\mathrm{e}}$ and $a_2 = a_{\mathrm{m}}$, as before.

2.6. Strain energy from axial compression

As shown in Figure 7, the main column is assumed to have a purely compressive displacement $\delta_c L$ and due to the high slenderness of the main column, it is assumed to be independent of $W(x)$. Hence the contribution to the strain energy U_{ca} is given by the expression:

$$U_{\mathrm{ca}} = \frac{1}{2} E_{\mathrm{c}} A_{\mathrm{c}} \int_0^{L} \delta_c^2 \, \mathrm{d}x. \tag{22}$$

The crossarms, in turn, are assumed to be inextensional and so the model is only in fact valid for the prestressed column system with an initial prestressing force in Zone 3 (see Figure 5), i.e. $T \geqslant T_{\mathrm{opt}}$, where all stays are in tension at the point of initial instability. The purpose for these assumptions is to simplify a highly complex system to one that is feasible to solve numerically. However, previous work has demonstrated conclusively that the system strength is maximized where $T > T_{\mathrm{opt}}$, as shown in the second graph of Figure 5. For lower prestressing levels, i.e. where $T < T_{\mathrm{opt}}$, the column has been deemed to be suboptimal either in terms of the load carrying capacity if T were very small or in terms of the post-buckling stability if T were less than but closer to T_{opt}, where the response was generally found to be more sensitive to imperfections without having the maximum increase in the critical buckling load [14, 15, 20].

2.7. Total potential energy

The total potential energy of the system comprises the strain energy stored minus the work done by the external load P. The strain energy comprises the axial energy of the main column, the bending energies of the main column and the crossarms alongside the strain energy stored from stretching the stays. Therefore the total potential energy V is obtained thus:

$$V = U_{\mathrm{ca}} + U_{\mathrm{cb}} + U_{\mathrm{s}} + \sum_{i=1}^{3} \left(U_{\mathrm{R}i} + U_{\mathrm{L}i} \right) - P\mathcal{E}, \tag{23}$$

where $\mathcal{E}$ is the column end displacement, thus:

$$\mathcal{E} = L \left(\delta_c + \Delta \right) \tag{24}$$

and ΔL is given by the well-known expression for the inextensional end-shortening of a strut [38], thus:

$$\Delta L = \frac{1}{2} \int_0^{L} W'^2 \, \mathrm{d}x. \tag{25}$$

Equilibrium states of the system are found by invoking the stationary potential energy criterion, hence:

$$\frac{\partial V}{\partial \delta_c} = 0, \quad \frac{\partial V}{\partial Q_j} = 0, \quad \frac{\partial V}{\partial Q_{\mathrm{R}k}} = 0, \quad \frac{\partial V}{\partial Q_{\mathrm{L}k}} = 0, \tag{26}$$

where the subscript j ranges from 1 to $2n$ (inclusive) and the subscript k ranges from 1 to 3 (inclusive). The first equation gives the pre-buckling path:

$$\delta_c = \frac{P}{E_{\mathrm{c}} A_{\mathrm{c}}} \tag{27}$$

and the effective elimination of the passive coordinate δ_c. The remaining expressions lead to a system of $2n+6$ simultaneous nonlinear algebraic equations that are formulated within the symbolic computation package Maple [39] and are subsequently solved numerically using the continuation and bifurcation software AUTO-07P [21]. AUTO is a well-known and powerful nonlinear solver that has the advantage of retaining the bifurcational structure of the system equations, it also computes how the solutions evolve with parametric variations and it has the facility to switch between different solution branches.

3. Finite element modelling

A finite element (FE) model developed within the commercial package ABAQUS [33] is also implemented. The purpose of the FE model is two-fold, firstly to calibrate the crossarm shape functions used in the analytical model for linear buckling analysis and, secondly, to validate the subsequent nonlinear post-buckling results from the analytical model. The column and the crossarms are modelled with beam elements and the stays are modelled with truss elements. In the same way as the analytical model, the simply supported column and its crossarms are connected rigidly, whereas the stays are pinned to the ends of the column and the crossarms. The 'No Compression' option within ABAQUS is enabled within the software to ensure that the stays are able to carry only tensile forces. To investigate the post-buckling behaviour, linear eigenvalue analysis is conducted first to obtain the distinct buckling loads and eigenmodes. The buckling loads are used to evaluate the theoretical optimal prestressing force T_{opt}, as described in §2.1. The buckling loads are also used to calibrate the parameter κ that was introduced in Eq. (9). With the introduction of the prestress within the stays and a small imperfection that comprises a linear combination of the eigenmodes, the nonlinear Riks arclength method [40] is used within ABAQUS to investigate the post-buckling behaviour. Comparisons are made with the analytical model for a variety of different cases for validation purposes.

4. Results and discussion

To conduct the parametric study, the material and geometric properties that are fixed are presented in Table 1, the numerical values of which are primarily based on previous studies [13, 14]. The crossarm length ratio $\gamma = a_{\mathrm{e}}/a_{\mathrm{m}} = 0.8$ and the prestressing force in the stays $T = T_{\mathrm{opt}}$ are also fixed for the most part, but are varied at specific points in the

Table 1: Material properties and structural dimensions of the triple-bay prestressed stayed columns.

Young's modulus of the main column and crossarms	$E_{\mathrm{c}} = E_{\mathrm{a}} = 201$ kN/mm^2
Crossarms Young's modulus	$E_{\mathrm{a}} = 201$ kN/mm^2
Young's modulus of the stays	$E_{\mathrm{s}} = 202$ kN/mm^2
Outside diameter of the main column and crossarms	$\phi_{\mathrm{co}} = \phi_{\mathrm{ao}} = 38.1$ mm
Inside diameter of the main column and crossarms	$\phi_{\mathrm{ci}} = \phi_{\mathrm{ai}} = 25.4$ mm
Length of the main column	$L = 5080$ mm
Yield stress of the main column	$f_{\mathrm{y}} = 355$ N/mm^2
Normalized slenderness of the main column	$\bar{\lambda} = 5.94$
Euler buckling load of the main column	$P_{\mathrm{E}} = 6.38$ kN

investigation. The normalized slenderness of the main column element $\bar{\lambda}$ is defined by the well known expression [41]:

$$\bar{\lambda} = \sqrt{P_{\mathrm{y}}/P_{\mathrm{E}}}, \tag{28}$$

with P_{y} being the squash load and P_{E} being the Euler buckling load of the main column element, where:

$$P_{\mathrm{y}} = A_{\mathrm{c}} f_{\mathrm{y}}, \quad P_{\mathrm{E}} = \frac{\pi^2 E_{\mathrm{c}} I_{\mathrm{c}}}{L^2}. \tag{29}$$

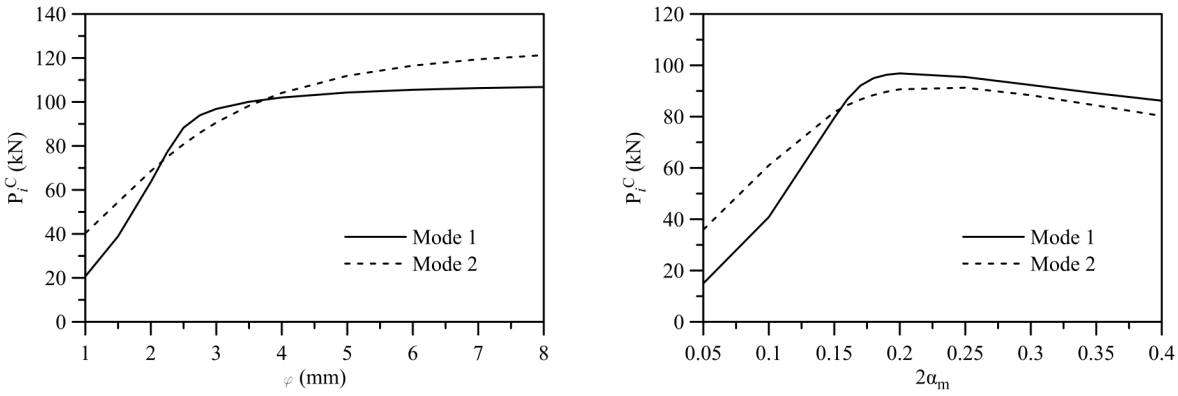
Two parameters, the stay diameter ϕ_{s} and the middle crossarm length a_{m}, are varied extensively in the current study. While investigating the effect of varying ϕ_{s}, the ratio $2\alpha_{\mathrm{m}}$ is fixed to 0.2; whereas while $2\alpha_{\mathrm{m}}$ is varied ϕ_{s} is fixed to 3 mm.

4.1. Buckling loads

In the current study, eight generalized coordinates are introduced to describe the main column shape to meet both the requirements of computational efficiency and model accuracy (from Eq. (5): $n = 4$); the shape therefore comprises four symmetric alongside four antisymmetric component waves. The model has therefore a total of 14 degrees of freedom plus the purely compressive displacement component δ_{c}.

In previous work [14], the analytical prediction of the antisymmetric buckling load was relatively poor as compared to the corresponding symmetric buckling load. Hence the parameter κ, which was introduced in Eq. (9), is parametrized and compared numerically against the FE model formulated within ABAQUS. For the current geometry, it was determined that a good prediction was found for $\kappa = 0.55$, where the analytical and FE buckling loads for Mode 2 first coincide with Mode 1 at the same values of ϕ_{s} and $2\alpha_{\mathrm{m}}$. Hence this value is used in all the subsequent analytical results presented. However, if the size of the main column cross-section were to be changed relative to those of the crossarms, it is likely that κ would need re-calibration.

Figure 8 shows the linear buckling loads with both the stay diameter ϕ_{s} and the middle crossarm length $2\alpha_{\mathrm{m}}$ varying. While ϕ_{s} varies, Mode 1 is critical when ϕ_{s} is small. Along with the increase of the stay diameter ϕ_{s}, the buckling loads of Modes 1 and 2 become closer and intersect at approximately $\phi_{\mathrm{s}} = 2.5$ mm. Mode 2 then becomes critical until ϕ_{s} reaches 3.8 mm, where Mode 1 becomes critical once again. Similarly, while $2\alpha_{\mathrm{m}}$ varies



(a) ϕ_{s} varying

(b) $2\alpha_{\mathrm{m}}$ varying

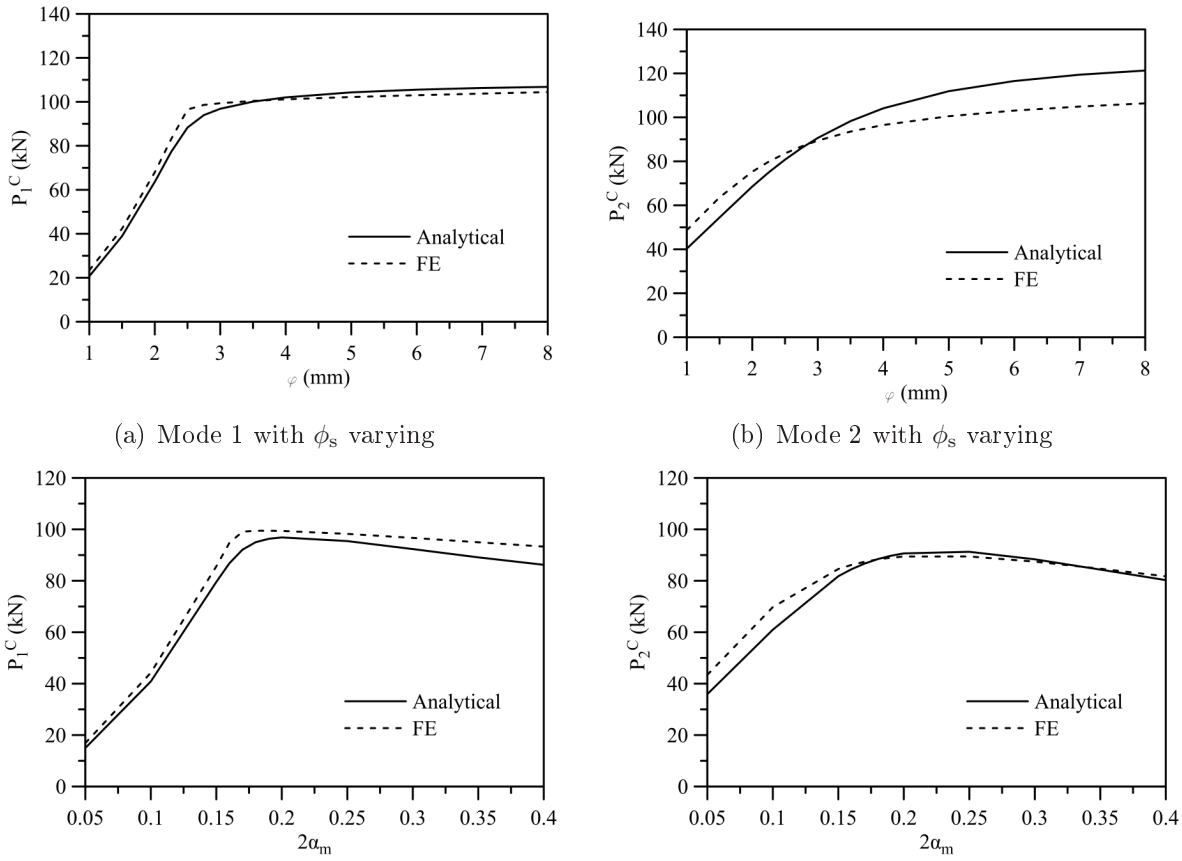
Figure 8: Buckling loads P_i^{C} for Mode i obtained from the analytical model with (a) the stay diameter ϕ_{s} and (b) the middle crossarm length $2\alpha_{\mathrm{m}}$ varying.

Mode 1 governs initially until $2\alpha_{\mathrm{m}}$ is approximately 0.15; subsequently Mode 2 is critical for higher values of $2\alpha_{\mathrm{m}}$.

Figure 9 shows the comparisons of the buckling loads between the analytical and FE models with both ϕ_{s} and $2\alpha_{\mathrm{m}}$ varying. The comparisons show excellent agreement especially for Mode 1, owing to the fact that the middle crossarms during Mode 1 buckling do not bend. The results justify the numerical selection of κ. It is also noteworthy that the stayed system increases the critical buckling load by up to a factor of approximately 15 for the considered configuration. However, given that the normalized slenderness of the main column is 5.94, the critical buckling load of the prestressed stayed system only reaches up to approximately 50% of the squash load P_{y} of the main column element, which in the current case is 225 kN. Hence the assumption of purely elastic behaviour is justified as in previous work [7, 18, 42, 34], and the investigation of the effect of material yielding is left for future work.

4.2. Nonlinear buckling

The principal focus of the current study concerns the post-buckling behaviour. Apart from buckling with purely Mode 1 or Mode 2 being triggered, interactive buckling is also observed in the equilibrium path especially when the buckling loads of Modes 1 and 2 are very close. Figure 10 shows the equilibrium paths of the applied axial load P versus the column end displacement $\mathcal{E}$ with $\phi_{\mathrm{s}} = 3$ mm while $2\alpha_{\mathrm{m}}$ is varied. When $2\alpha_{\mathrm{m}}$ is relatively small, such as when $2\alpha_{\mathrm{m}} = 0.1$, Mode 1 governs throughout the post-buckling stage. As $2\alpha_{\mathrm{m}}$ is increased, the paths of Modes 1 and 2 become closer and both ultimate load capacities increase. When $2\alpha_{\mathrm{m}} = 0.175$, where Mode 2 is marginally critical and the ultimate load capacities of both pure modes are very close, interactive buckling can be observed, see Figure 10(c), which bifurcates from Mode 2, then becomes dominant before the equilibrium path intersects the path of pure Mode 1. When $2\alpha_{\mathrm{m}}$ increases further, Mode 2 still governs critical buckling but the interactive path leading eventually to Mode



(a) Mode 1 with ϕ_s varying

(b) Mode 2 with ϕ_s varying

(c) Mode 1 with $2\alpha_m$ varying

(d) Mode 2 with $2\alpha_m$ varying

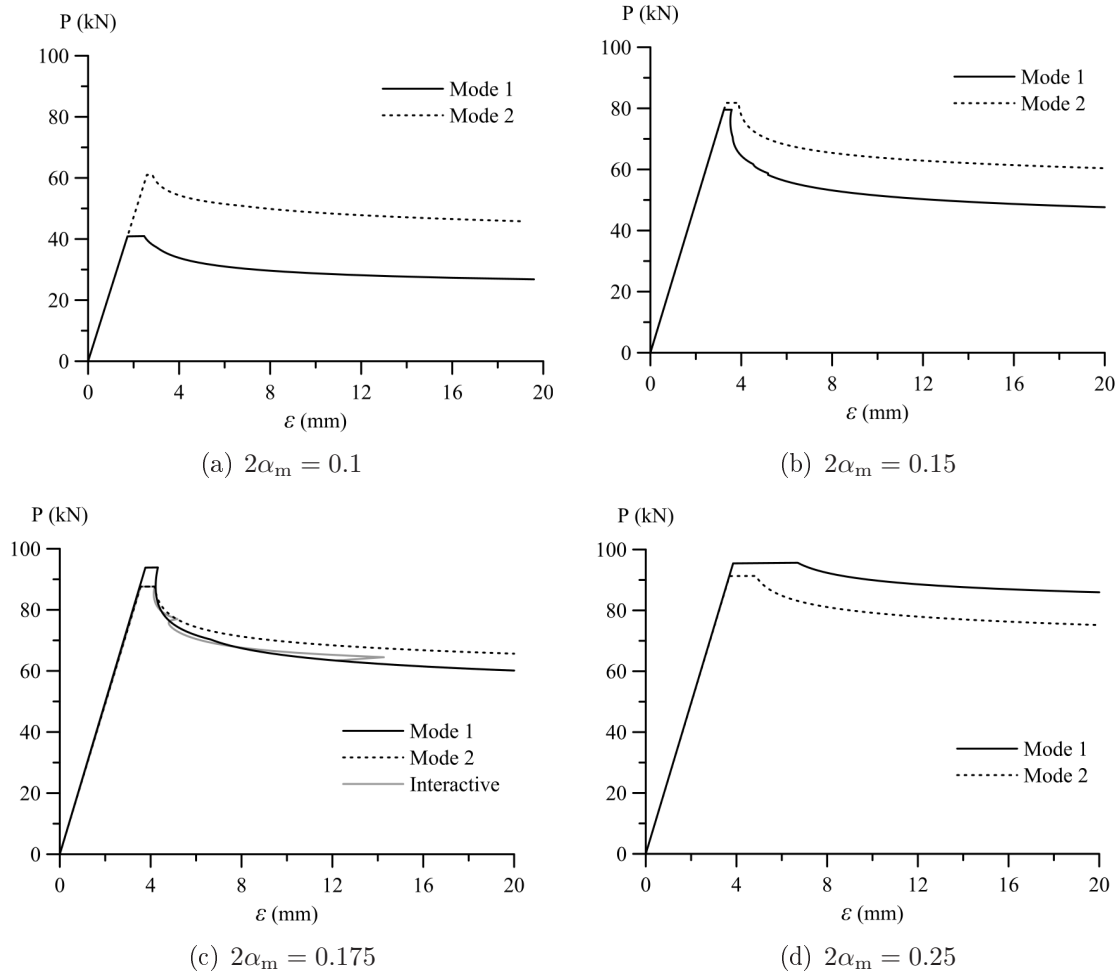
Figure 9: Comparisons of the obtained buckling loads evaluated using the analytical and FE models for Mode 1 (P_1^C) and Mode 2 (P_2^C) with the stay diameter ϕ_s and middle crossarm length $2\alpha_m$ varying.

1 is not observed.

Similarly, Figure 11 shows the equilibrium paths of the axial load P versus the column end displacement $\mathcal{E}$ with $2\alpha_m = 0.2$ while ϕ_s is varied. When the stay diameter ϕ_s is small, Mode 1 governs throughout the post-buckling stage. As ϕ_s is increased, the ultimate load capacities of Modes 1 and 2 become closer and eventually Mode 2 begins to govern. Again, this time when $\phi_s = 2.5$ mm, interactive buckling is observed; it dominates the behaviour for a while before the path eventually returns to Mode 1. Cases with $2\alpha_m$ and ϕ_s varying imply that when the critical loads of Modes 1 and 2 are very close and Mode 2 is critical, the actual post-buckling behaviour is governed by mode interaction. This observation concurs precisely with previous FE studies for the single-bay [16] and the triple-bay cases [43].

4.2.1. Mode interaction

Figures 10 and 11 demonstrate that interactive buckling is observed when the buckling loads of Modes 1 and 2 are close and is considered to be the most dangerous scenario. The process for how the two modes interact is now discussed. Initially when ϕ_s or $2\alpha_m$

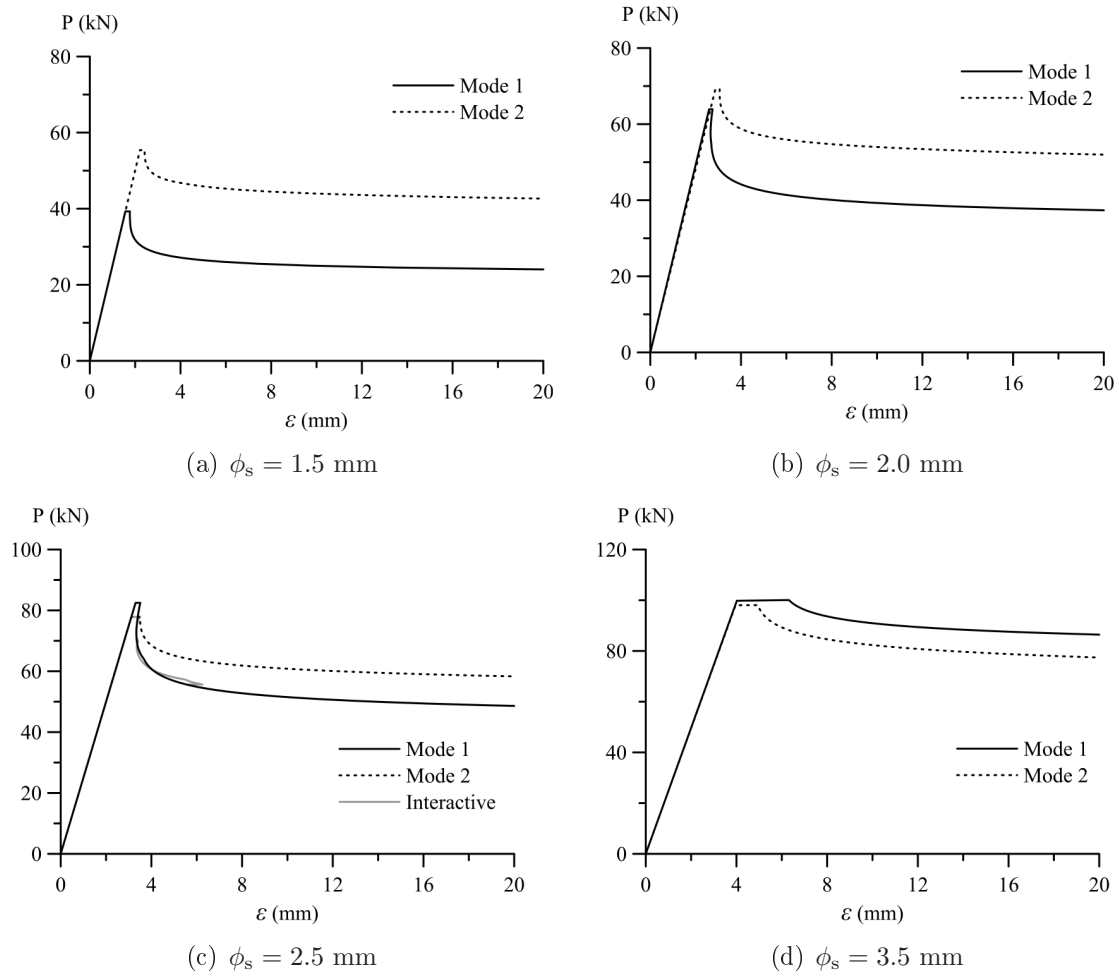


(a) $2\alpha_{\mathrm{m}} = 0.1$ (b) $2\alpha_{\mathrm{m}} = 0.15$

(c) $2\alpha_{\mathrm{m}} = 0.175$ (d) $2\alpha_{\mathrm{m}} = 0.25$

Figure 10: Equilibrium paths of the applied load P versus the column end displacement $\mathcal{E}$ with $2\alpha_{\mathrm{m}}$ varying while $\phi_{\mathrm{s}} = 3$ mm and $\gamma = 0.8$. All results are obtained from the analytical model.

is small, the ultimate load capacity of Mode 2 is significantly larger than that of Mode 1 and only pure modes are observed during post-buckling. Along with the increase of ϕ_{s} or $2\alpha_{\mathrm{m}}$, when Mode 1 is still critical but the load capacities of the two pure modes are close, a pair of passive interaction loops can be observed orbiting the pure Mode 1 branch, as shown in Figure 12(a). At the instance when the buckling load of Mode 1 exceeds that of Mode 2, the passive interaction loop orbiting the pure Mode 1 post-buckling path is replaced with a fully interactive buckling path with a characteristic loop that connects the post-buckling paths of both pure Modes 1 and 2, see Figure 12(c), which was also predicted in a much more simplified model comprising rigid links and discrete springs in previous work [17]. The process begins by triggering Mode 2 at the first bifurcation point B_1, then coordinate Q_2 grows with $Q_1 = 0$ until the second bifurcation point B_2 beyond which interactive buckling is triggered and Q_1 grows alongside Q_2. The path eventually returns to Mode 1 at the third bifurcation point B_3. The complete process is also known



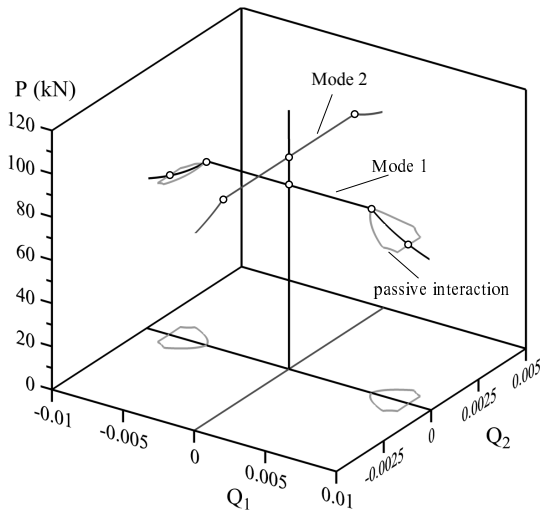
(a) $\phi_{\mathrm{s}} = 1.5$ mm (b) $\phi_{\mathrm{s}} = 2.0$ mm

(c) $\phi_{\mathrm{s}} = 2.5$ mm (d) $\phi_{\mathrm{s}} = 3.5$ mm

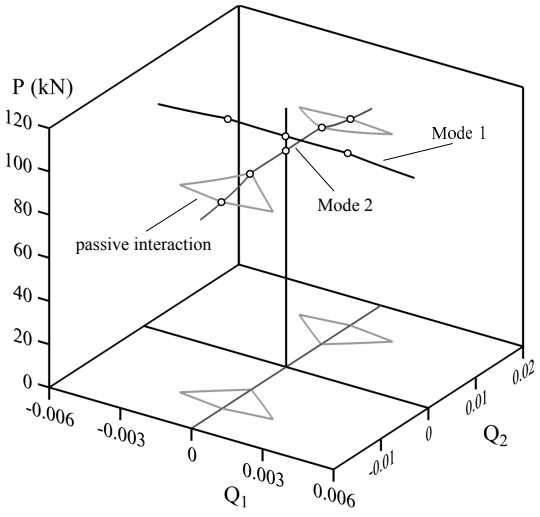
Figure 11: Equilibrium paths of the applied load P versus the column end displacement $\mathcal{E}$ with ϕ_{s} varying while $2\alpha_{\mathrm{m}} = 0.2$ and $\gamma = 0.8$. All results are obtained from the analytical model.

as 'mode jumping' [44]. This interactive post-buckling response is in fact the dominant behaviour, even though Mode 2 is critical, and the load carrying capacity is seen to reduce substantially during this process. Moreover, there is a sequence of potentially explosive snap-backs in the mechanical response where there are discontinuities in slope; these are signatures of the stays slackening sequentially on the concave side of the buckling column and may be considered to produce a 'cellular buckling' [27, 31] or 'snaking' response [45, 46]. If ϕ_{s} or $2\alpha_{\mathrm{m}}$ are increased further and Mode 2 remains critical but the difference in the load capacities of the two distinct modes is larger, the full interaction between Modes 1 and 2 is no longer observed. Instead, a pair of passive interaction loops can be observed orbiting the pure Mode 2 post-buckling path, see Figure 12(b), in precisely the same way as they had existed in Figure 12(a) orbiting the pure Mode 1 post-buckling path.

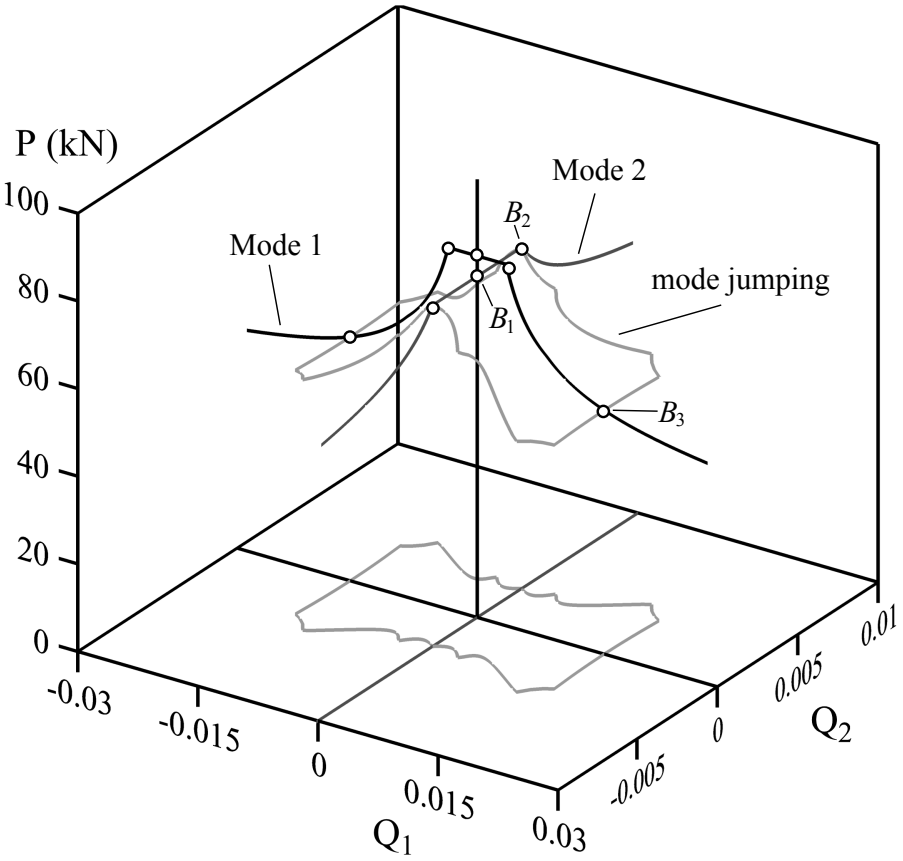
Figure 13 shows the distribution of Q_1 versus Q_2 with $2\alpha_{\mathrm{m}}$ varying from 0.175 to 0.2, where the value of the Mode 1 buckling load just exceeds that of Mode 2, but is still very



(a) Passive interaction orbiting Mode 1

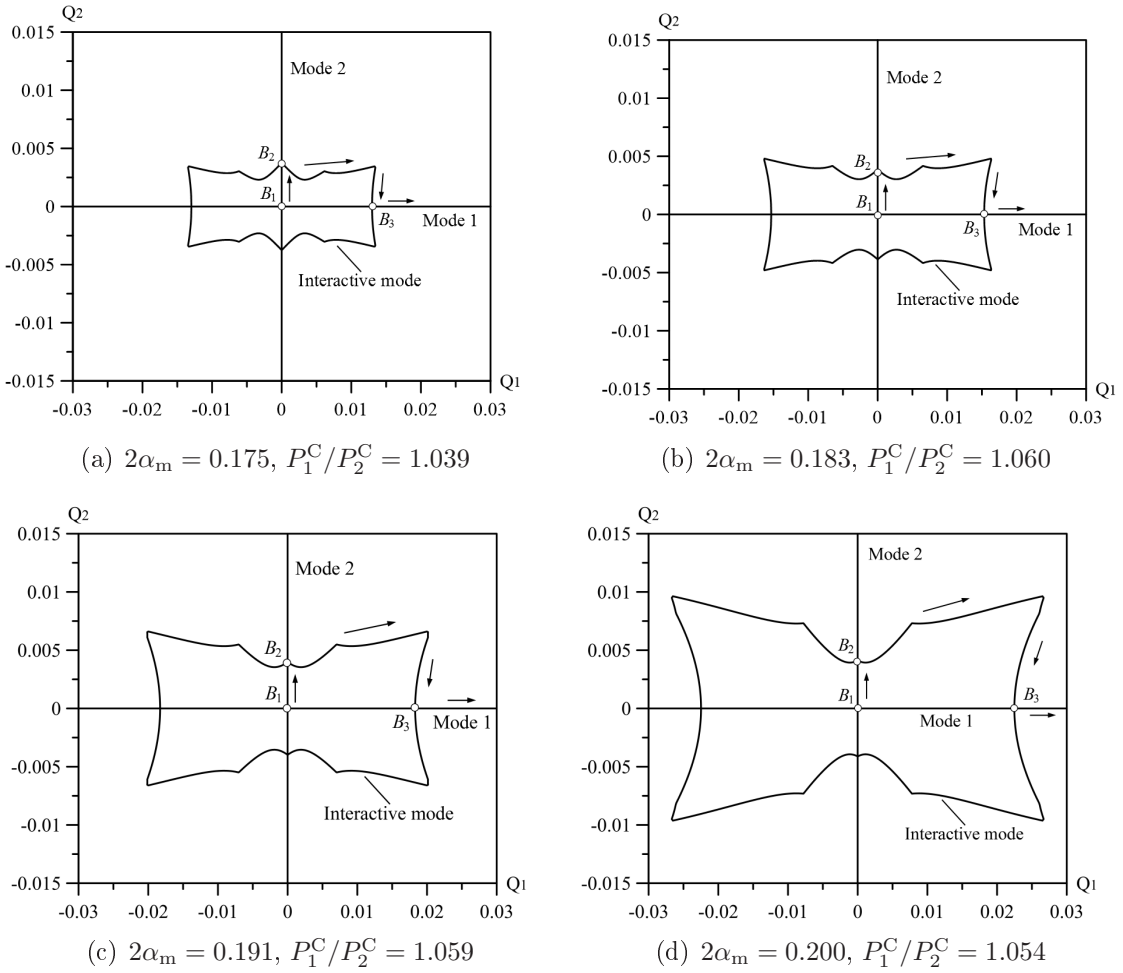


(b) Passive interaction orbiting Mode 2



(c) Full interaction: mode jumping from Mode 2 to Mode 1

Figure 12: Three-dimensional plots of the equilibrium paths of P versus Q_1 and Q_2 with $2\alpha_{\rm m} = 0.2$, $\gamma = 0.8$ and (a) $\phi_{\rm s} = 1.5$ mm, (b) $\phi_{\rm s} = 3.0$ mm and (c) $\phi_{\rm s} = 2.5$ mm; (a) and (b) show passive interactions orbiting individual Modes 1 and 2 respectively, whereas (c) shows a full interaction loop connecting both Modes 1 and 2 with the mode jumping from Mode 2 to Mode 1 in a single process.



(a) $2\alpha_{\mathrm{m}} = 0.175$, $P_1^{\mathrm{C}}/P_2^{\mathrm{C}} = 1.039$

(b) $2\alpha_{\mathrm{m}} = 0.183$, $P_1^{\mathrm{C}}/P_2^{\mathrm{C}} = 1.060$

(c) $2\alpha_{\mathrm{m}} = 0.191$, $P_1^{\mathrm{C}}/P_2^{\mathrm{C}} = 1.059$

(d) $2\alpha_{\mathrm{m}} = 0.200$, $P_1^{\mathrm{C}}/P_2^{\mathrm{C}} = 1.054$

Figure 13: Equilibrium paths of Q_1 versus Q_2 when $\phi_{\mathrm{s}} = 3$ mm and $\gamma = 0.8$ with increasing $2\alpha_{\mathrm{m}}$ showing different sizes of interactive buckling loops and paths where the mode jumping process occurs.

close. It can be seen that the size of the interactive loop becomes larger, along with the increase of $2\alpha_{\mathrm{m}}$, as the practical effect of mode interaction becomes less significant since $2\alpha_{\mathrm{m}}$ values are further away from the point where the critical loads coincide, as shown in Figure 8(b). The loop, in fact, eventually breaks at a certain point, after which the fully interactive behaviour is not observed in the analytical model and only passive interactions with the paths orbiting individual pure modes are observed, as shown in Figure 12(a–b).

Figure 14 shows the sequence of behaviour that depicts the stage-by-stage transformation of the buckling shape in the mode jumping process. Initially, the system hits the first bifurcation point B_1 and Q_2 grows towards the second bifurcation point B_2, see Figure 14(a). Since $Q_1 = 0$ and all of the stays are in tension, the buckling forms as the purely antisymmetric shape (Mode 2) at this stage. When the path reaches the bifurcation point B_2, the strain in the first stay on the concave side (stay 8 as depicted – see Figure 3(a) for stay label definitions) just decreases to zero simultaneously, it becomes slack and mode

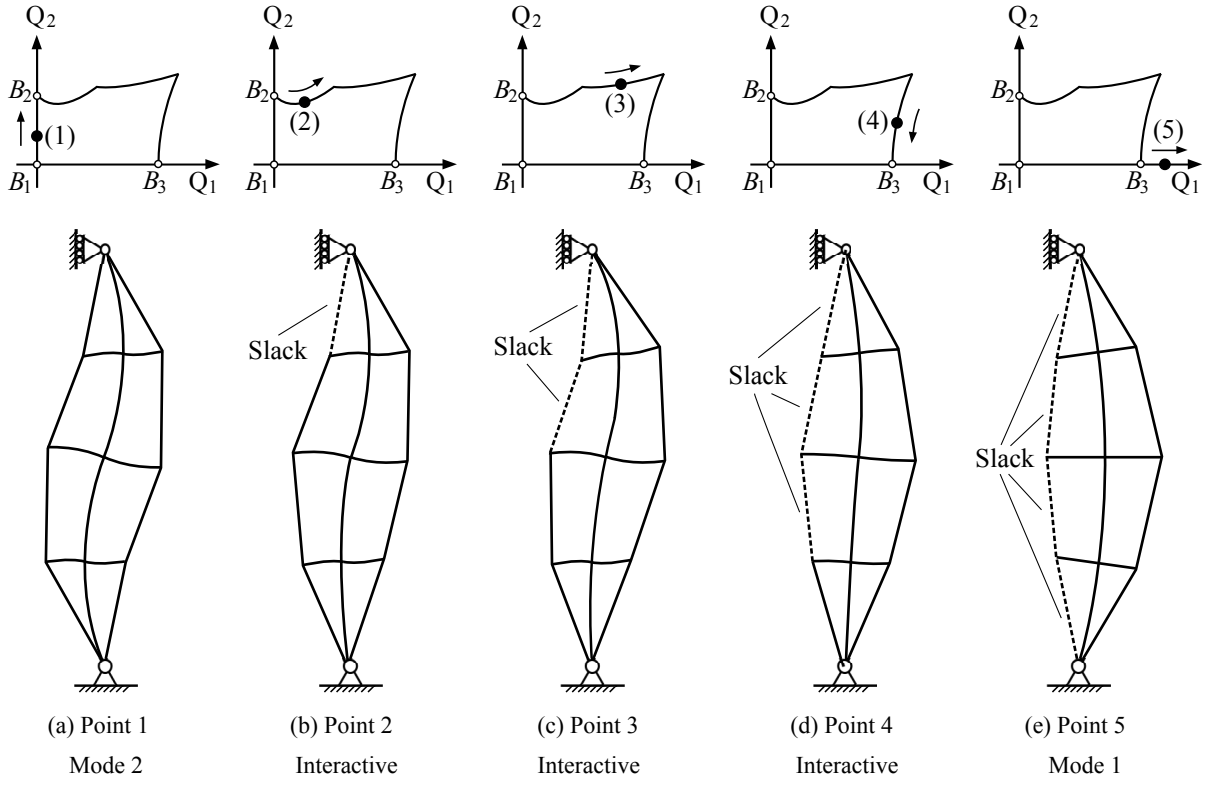


Figure 14: The detailed transformation of the post-buckling profile in the nonlinear mode jumping process. The solid circle shows the combination of Q_1 and Q_2 for the corresponding deformation profile shown in (a–e).

interaction is first triggered, see Figure 14(b). When the path passes the next slope discontinuity, another stay goes slack (stay 7 as depicted), as shown in Figure 14(c). Once the path reaches the top-right corner of the interactive loop, the third stay becomes slack (stay 6 as depicted) and from this point, the buckling shape more or less resembles Mode 1 rather than Mode 2, as shown in Figure 14(d). Finally, when the path eventually arrives at B_3, the mode jumping process finishes and the transformation from pure Mode 2 to pure Mode 1 is complete, as shown in Figure 14(e) with the final stay going slack (stay 5 as depicted).

Owing to the fact that when interactive buckling leads to mode jumping the structural component has the most severely unstable response, it is of paramount practical importance to determine in which combinations of system parameters this occurs. Passive Mode 1 interaction occurs when Mode 1 is critical but the load capacities of Modes 1 and 2 are close, see Figure 12(a). The size of the passive loop becomes larger along with the increase of ϕ_{s} or $2\alpha_{\mathrm{m}}$ and the passive interaction is replaced by full interaction with mode jumping when Mode 2 just becomes critical. The mode jumping interaction loop becomes larger along with the increase of ϕ_{s} or $2\alpha_{\mathrm{m}}$, as shown in Figure 13, and eventually breaks where it is replaced by passive Mode 2 interaction, see Figure 12(b). Unlike the passive Mode

1 interaction and the full mode jumping interaction, the passive Mode 2 interaction loop becomes smaller along with the increase of ϕ_s or $2\alpha_m$. In the current study, when the amplitude of Q_1 within the passive Mode 2 interaction loop is smaller than 0.0025, it is assumed that the contribution of the symmetric mode is very small, the passive interaction is deemed to be negligible and the buckling mode is considered to be purely Mode 2. This size of lateral midspan deflection, measured as $Q_1 L$, defined as $L/400$, is in accord with manufacturing tolerances for the design of structural steel components [47].

Figure 15 shows the configurations where mode jumping and the passive interactions are

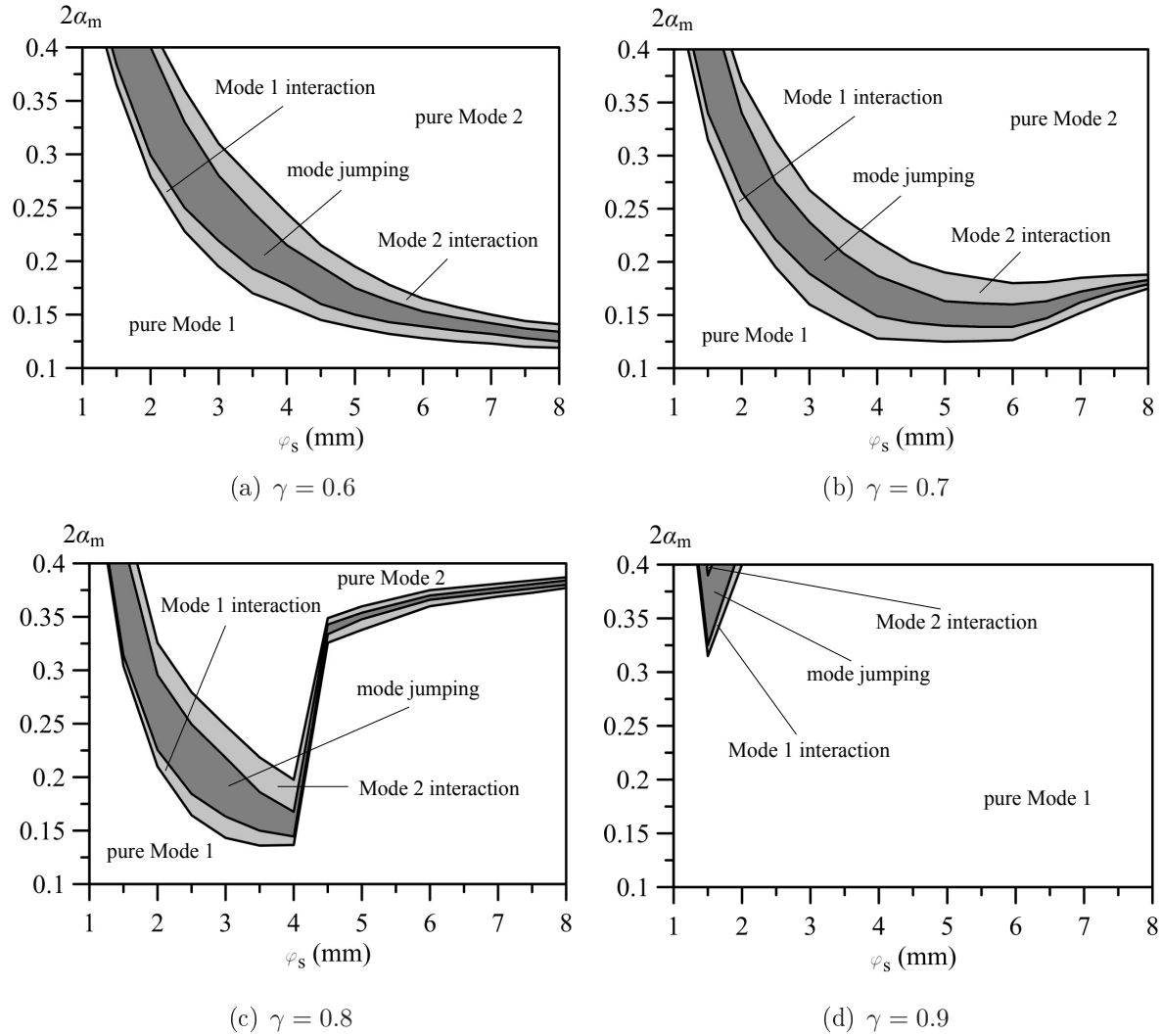
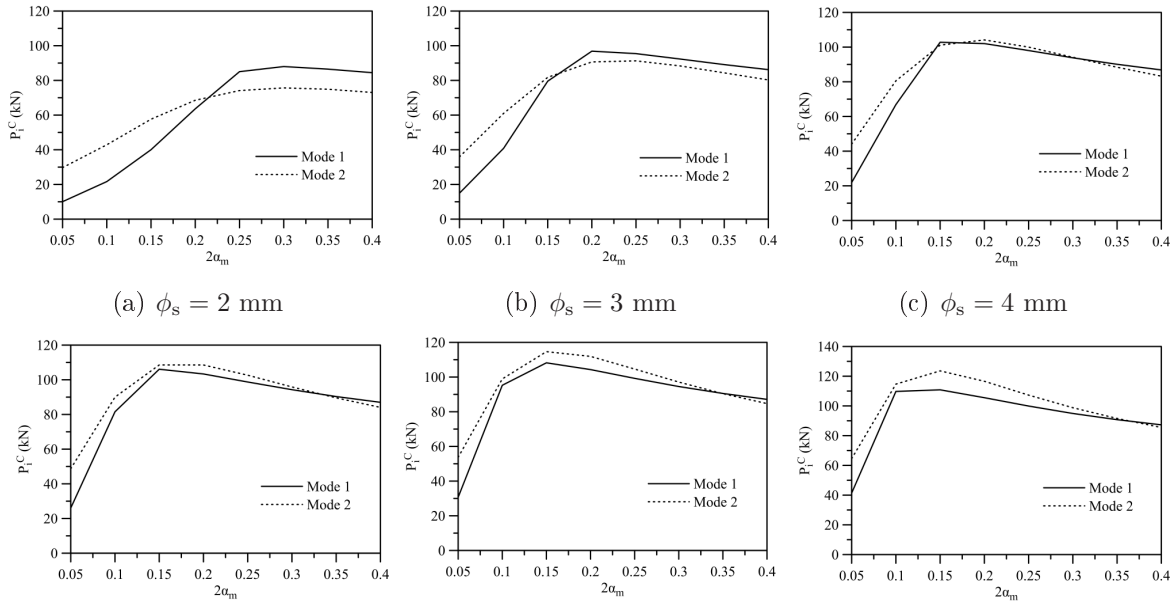


Figure 15: Parametric spaces of $2\alpha_m$, ϕ_s and γ showing regions where mode interactions that cause mode jumping (i.e. full interaction between Modes 1 and 2 with cellular buckling) and passive interactions.

significant with the stay diameter ϕ_s, the ratio $2\alpha_m$ and the crossarm length ratio γ varying. It can be seen that there is a wider range of configurations where interactive buckling occurs with relatively small ϕ_s and large $2\alpha_m$ values. When $\gamma = 0.6$ and 0.7, the parametric space

of mode jumping and passive interaction ranges from the region with large $2\alpha_{\mathrm{m}}$ and small ϕ_{s} values to the region with small $2\alpha_{\mathrm{m}}$ and large ϕ_{s} values relatively smoothly. When $\gamma = 0.8$, which is the value used for most of the presented results in the current work, it can be seen from Figure 16 that the point of coincidence for buckling loads of Modes 1 and



(a) $\phi_{\mathrm{s}} = 2$ mm (b) $\phi_{\mathrm{s}} = 3$ mm (c) $\phi_{\mathrm{s}} = 4$ mm

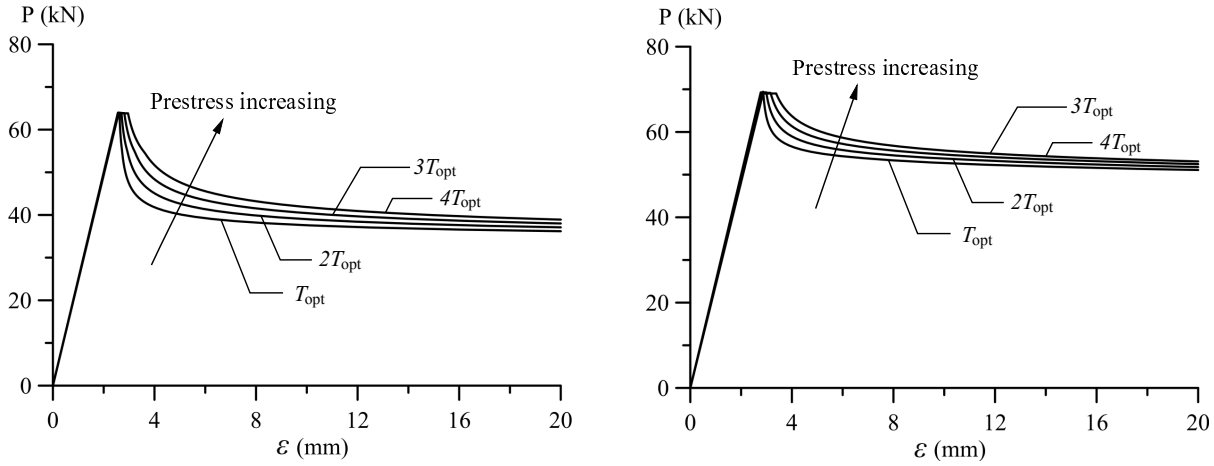
(d) $\phi_{\mathrm{s}} = 4.5$ mm (e) $\phi_{\mathrm{s}} = 5$ mm (f) $\phi_{\mathrm{s}} = 6$ mm

Figure 16: The buckling loads of Modes 1 and 2 with $2\alpha_{\mathrm{m}}$ and ϕ_{s} varying while $\gamma = 0.8$.

2 changes dramatically from $2\alpha_{\mathrm{m}}$ being approximately 0.15 to approximately 0.34 while increasing ϕ_{s} from 3 mm to 4.5 mm. Therefore a significant change in the parametric space of mode jumping and passive pure mode interaction is observed in this range. This change can be attributed to the sudden change in the position of the intersection of the linear buckling loads, as seen in Figures 16(b) and 16(d). It can also be seen that when $\gamma = 0.9$, interactive buckling only occurs at very small ϕ_{s} and very large $2\alpha_{\mathrm{m}}$ values, owing to the fact that Mode 2 is only critical for very large crossarm lengths. The reason for this is that the stay force component acting as a restraint on the main column through the midspan crossarms is relatively much lower in magnitude than for smaller values of γ presented in the graphs in Figure 15(a–c); this is simply related to the commensurate reduction in the angle β_{m} as shown in Figure 3(a).

4.3. Sensitivity to initial prestressing force

The benchmark prestressing force T_{opt}, used in all the results presented in the study hitherto, was evaluated through Eq. (1). As mentioned before, T_{opt} is derived purely from an elastic model based on linear eigenvalue analysis, which may not be the actual optimal prestressing force for the stayed column in terms of the true load carrying capacity and post-buckling stability. Figure 17 shows the equilibrium paths of the applied load P



(a) Mode 1 (b) Mode 2

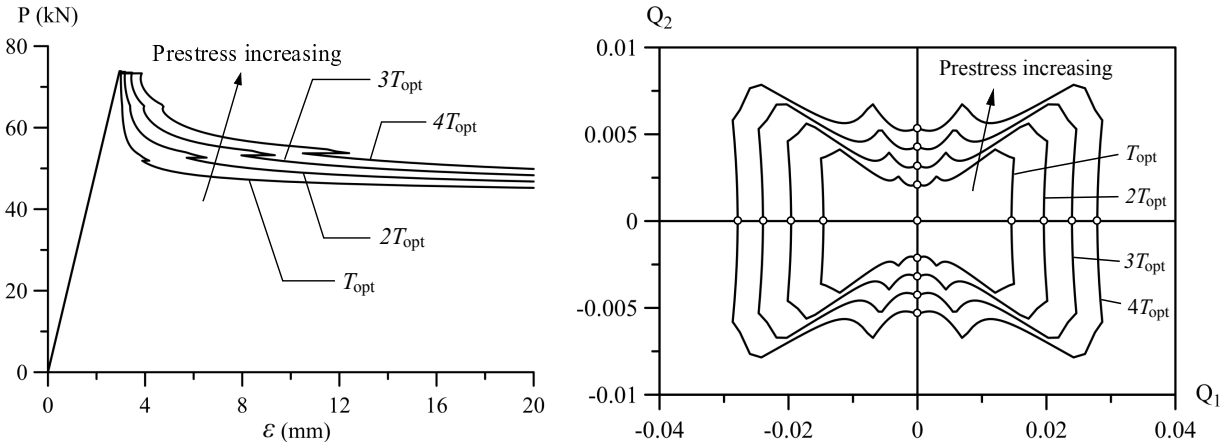
Figure 17: Equilibrium paths of the applied load P versus $\mathcal{E}$ with the prestress T varying while $\phi_{\rm s} = 2$ mm, $2\alpha_{\rm m} = 0.2$ and $\gamma = 0.8$. Note the increasing plateau size and the higher residual load in the initial and advanced post-buckling stages respectively with increasing T.

versus the end displacement $\mathcal{E}$ with the prestressing force T varying while $\phi_{\rm s} = 2$ mm, $2\alpha_{\rm m} = 0.2$ and $\gamma = 0.8$. It can be seen that in both cases for Modes 1 and 2, increasing the prestressing force from $T_{\rm opt}$ results in a very slight decrease in the load capacity but makes the post-buckling behaviour significantly more stable. This implies that the prestressed stayed column would benefit more from the prestressing force being larger than $T_{\rm opt}$. The investigation of determining the actual optimal prestressing force is left for future work, but it is noted that it would be significantly higher than $T_{\rm opt}$, as found for the single-bay case [19]. It is worth recalling that columns with prestressing forces less than $T_{\rm opt}$ would have significantly less buckling load capacities, as depicted in Figure 5.

Figure 18 shows the equilibrium paths of the interactive buckling case with the prestressing force T varying while $\phi_{\rm s} = 2.5$ mm and $2\alpha_{\rm m} = 0.2$. It can be seen that the interactive buckling loops become larger and the snap-backs become more pronounced along with the increasing of the prestressing force T. When the column is loaded axially and begins to deflect laterally, the stays on the concave side of the column need more deformation to eliminate the initial prestress and go slack since the initial strain is larger. As a result, the bifurcation points, where the stays go slack, are further away from the initial critical bifurcation point. The identical phenomenon can also be observed in Figure 17, where the distribution of the peak load plateau is extended by increasing the prestressing force from $T_{\rm opt}$. Of course, there is a limit on the level of the prestressing force T, which relates directly to the intrinsic compressive capacity of the main column element, either from elastic instability or material failure.

4.4. Validation of post-buckling results from analytical model

The same structural geometries and material properties are used in the FE model to conduct both linear and nonlinear analyses. Owing to the requirement of introducing

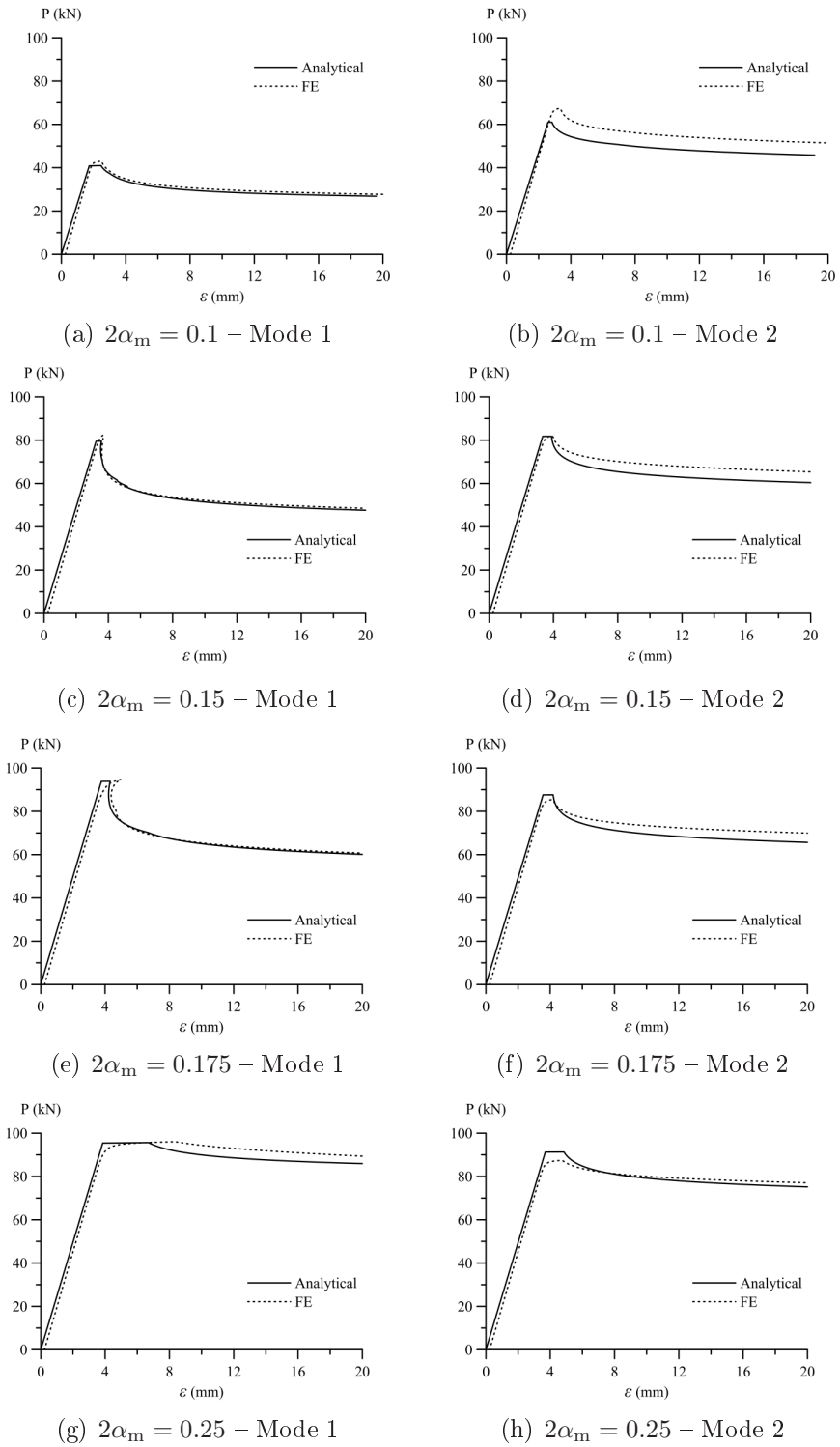


(a) P versus $\mathcal{E}$ (b) Q_1 versus Q_2

Figure 18: Equilibrium paths of the interactive buckling case with the prestressing force T varying while $\phi_{\rm s} = 2.5$ mm, $2\alpha_{\rm m} = 0.2$ and $\gamma = 0.8$. Note the increasing plateau size and the higher residual load in the initial and advanced post-buckling stages respectively with increasing T in (a).

imperfections as perturbations to obtain the near-perfect post-buckling response, an amplitude of $L/10000$ is selected to ensure a fair comparison with the analytical model. A mixture of the perturbations from the first two pure modes are used to trigger interactive buckling in the FE model. Figures 19 and 20 show the comparisons between equilibrium paths of the applied load P versus the column end displacement $\mathcal{E}$ for both $2\alpha_{\rm m}$ and $\phi_{\rm s}$ varying respectively. It is seen that the maximum load carrying capacity and the nonlinear post-buckling response compare excellently for all cases, especially for Mode 1 since the middle crossarms do not bend during symmetric buckling; hence there is less potential error introduced into the model from the shape functions of the crossarms.

Figure 21 shows the comparisons of two interactive buckling cases with mode jumping. The results show excellent agreement between the analytical and FE models, which implies the current analytical approach captures the interactive buckling behaviour both qualitatively and quantitatively. Figures 22 and 23 show the comparisons of the post-buckling profiles between the analytical and FE models at the peak load and when $\mathcal{E} = 20$ mm for $2\alpha_{\rm m} = 0.1$ and 0.25 while $\phi_{\rm s} = 3$ mm for pure Modes 1 and 2. The comparisons show excellent visual agreement in terms of buckling profile between the two models. Figures 24 and 25 show the corresponding comparisons of post-buckling profiles between the analytical and FE models at the peak load and the interactive buckling region with cases: (1) $2\alpha_{\rm m} = 0.2$ and $\phi_{\rm s} = 2.5$ mm; (2) $2\alpha_{\rm m} = 0.175$ and $\phi_{\rm s} = 3$ mm. The comparisons also show excellent visual agreement in terms of buckling profile at the peak load and when the column end displacement is small. Moreover, very good visual agreement is obtained when the column end displacement is relatively large. This, again, demonstrates that the analytical model established currently is quite capable of predicting the nonlinear behaviour accurately both qualitatively and quantitatively.



(a) $2\alpha_{\mathrm{m}} = 0.1$ – Mode 1

(b) $2\alpha_{\mathrm{m}} = 0.1$ – Mode 2

(c) $2\alpha_{\mathrm{m}} = 0.15$ – Mode 1

(d) $2\alpha_{\mathrm{m}} = 0.15$ – Mode 2

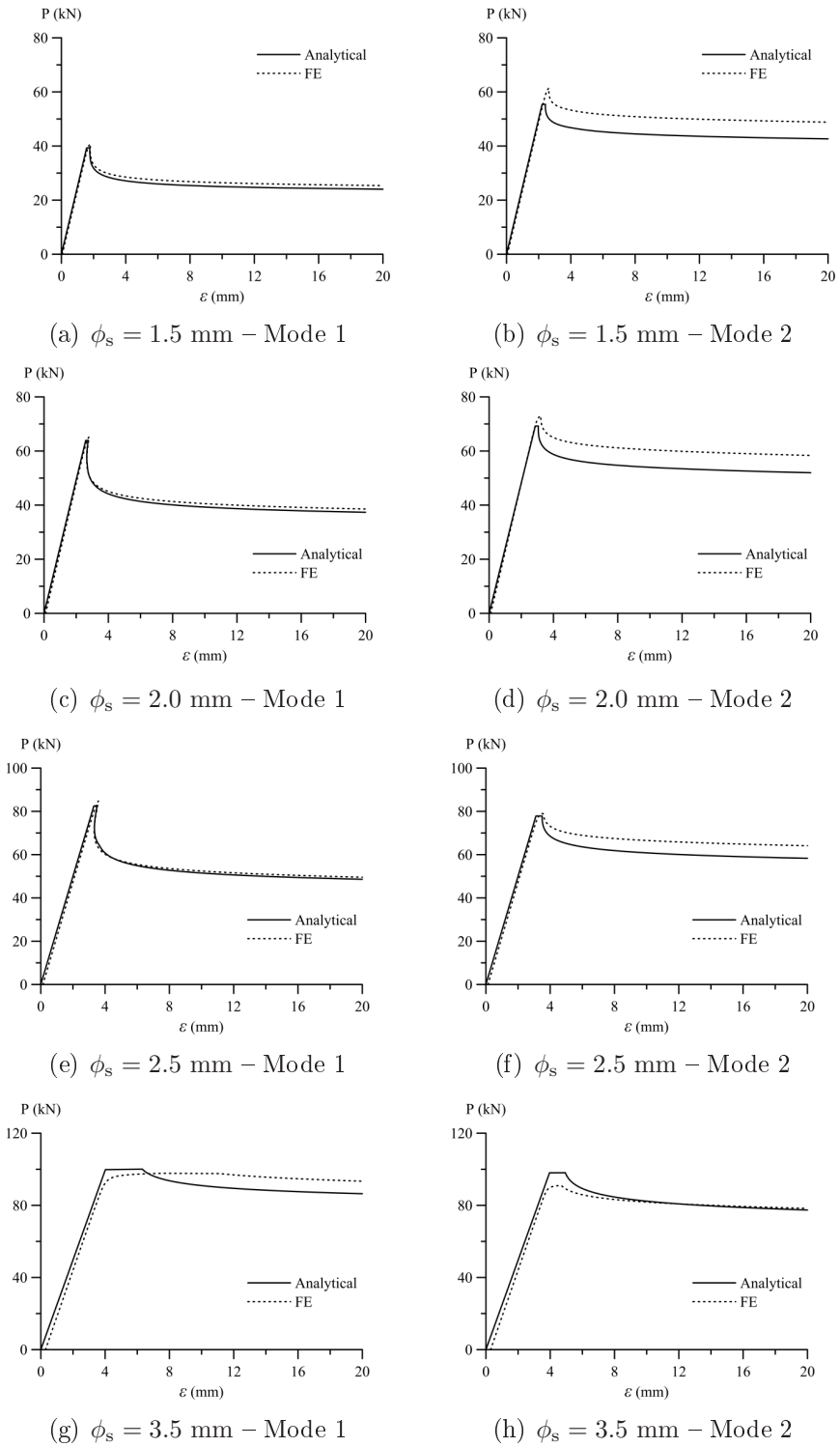
(e) $2\alpha_{\mathrm{m}} = 0.175$ – Mode 1

(f) $2\alpha_{\mathrm{m}} = 0.175$ – Mode 2

(g) $2\alpha_{\mathrm{m}} = 0.25$ – Mode 1

(h) $2\alpha_{\mathrm{m}} = 0.25$ – Mode 2

Figure 19: Comparisons of equilibrium paths of the applied load P versus the column end displacement $\mathcal{E}$ with $2\alpha_{\mathrm{m}}$ varying while $\phi_{\mathrm{s}} = 3$ mm and $\gamma = 0.8$. The graphs show the cases where (a, c, e and g) pure Mode 1 or (b, d, f and h) pure Mode 2 perturbations are introduced into the FE model.



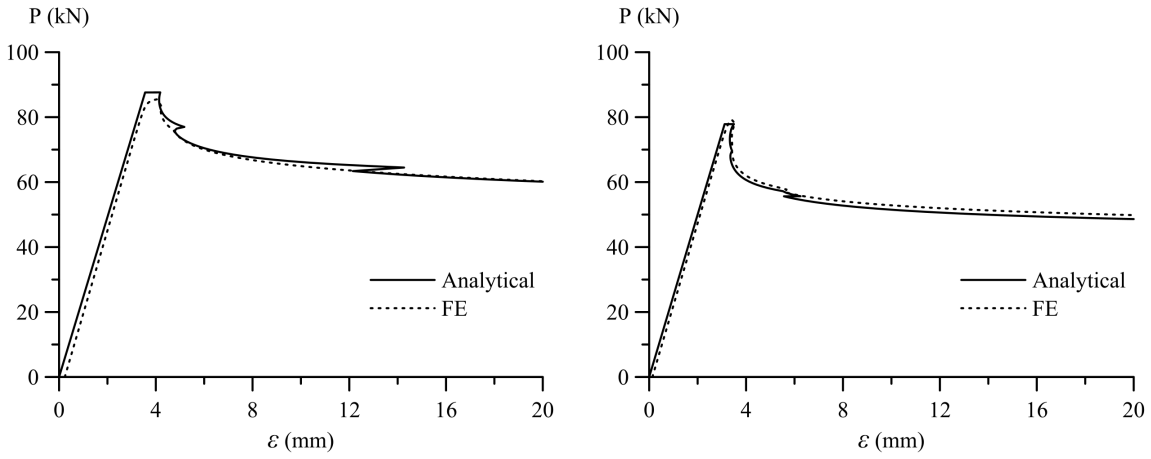
(a) $\phi_{\mathrm{s}} = 1.5$ mm – Mode 1 (b) $\phi_{\mathrm{s}} = 1.5$ mm – Mode 2

(c) $\phi_{\mathrm{s}} = 2.0$ mm – Mode 1 (d) $\phi_{\mathrm{s}} = 2.0$ mm – Mode 2

(e) $\phi_{\mathrm{s}} = 2.5$ mm – Mode 1 (f) $\phi_{\mathrm{s}} = 2.5$ mm – Mode 2

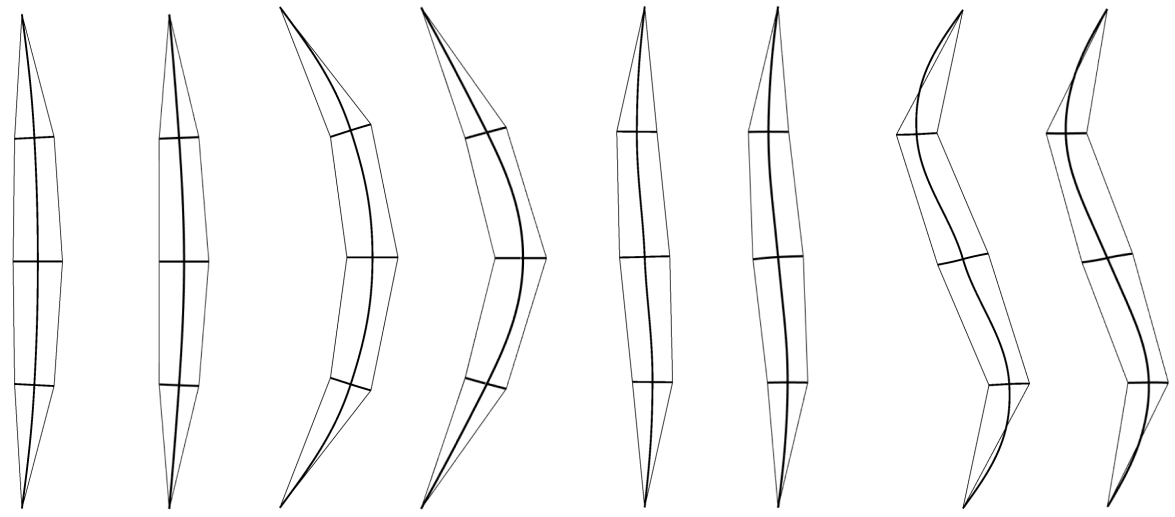
(g) $\phi_{\mathrm{s}} = 3.5$ mm – Mode 1 (h) $\phi_{\mathrm{s}} = 3.5$ mm – Mode 2

Figure 20: Comparisons of equilibrium paths of the applied load P versus the column end displacement $\mathcal{E}$ with ϕ_{s} varying while $2\alpha_{\mathrm{m}} = 0.2$ and $\gamma = 0.8$. The graphs show the cases where (a, c, e and g) pure Mode 1 or (b, d, f and h) pure Mode 2 perturbations are introduced into the FE model.



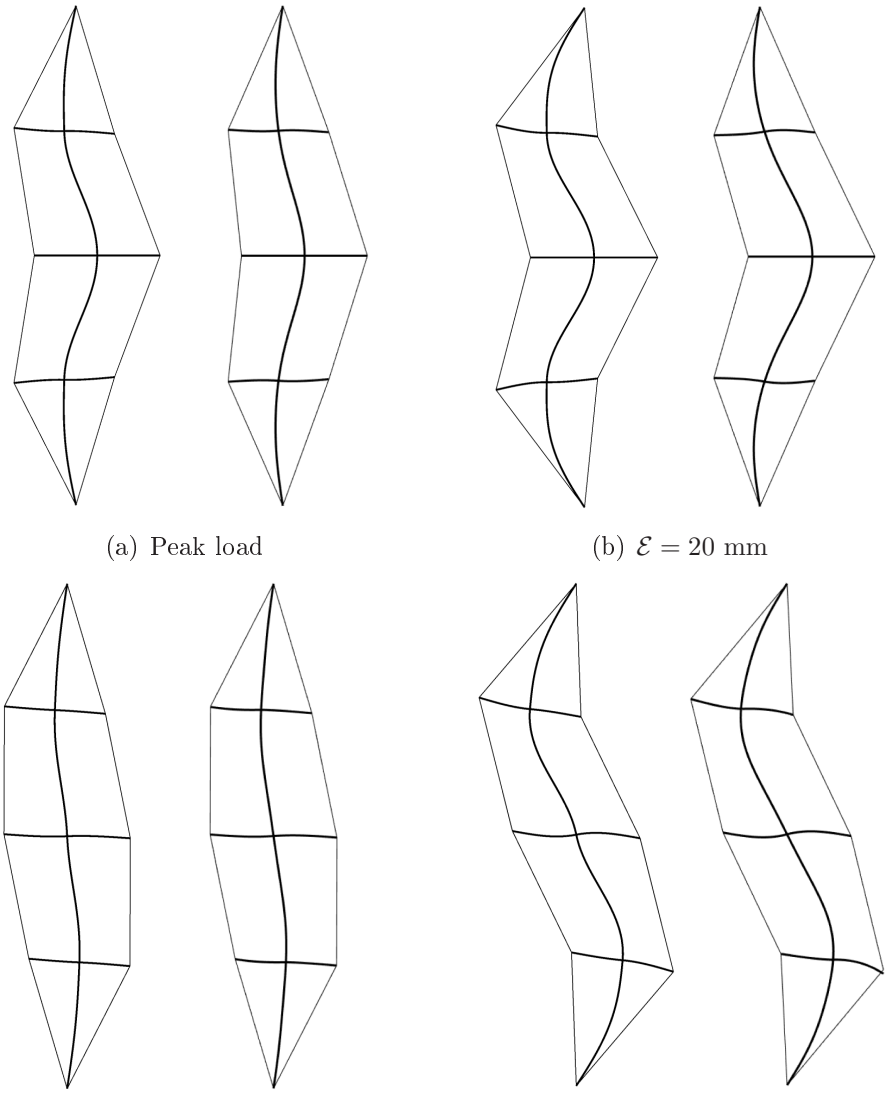
(a) $\phi_{\mathrm{s}} = 3$ mm and $2\alpha_{\mathrm{m}} = 0.175$ (b) $\phi_{\mathrm{s}} = 2.5$ mm and $2\alpha_{\mathrm{m}} = 0.2$

Figure 21: Comparisons of equilibrium paths of the applied load P versus the column end displacement $\mathcal{E}$ for the cases exhibiting interactive buckling. In this case, the FE model has a combination of Modes 1 and 2 for the initially perturbed shape and $\gamma = 0.8$.



(a) Peak load (b) $\mathcal{E} = 20$ mm (c) Peak load (d) $\mathcal{E} = 20$ mm

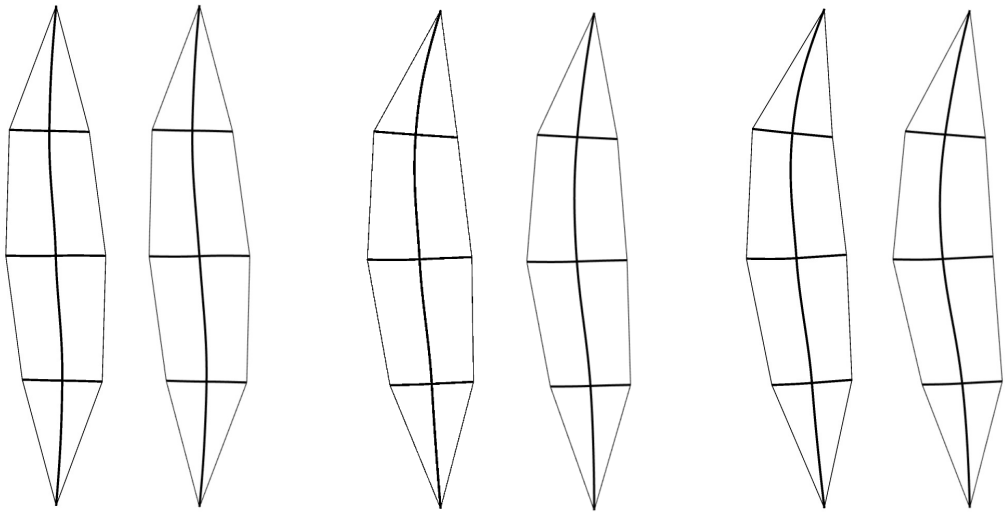
Figure 22: Comparisons of post-buckling profiles between the analytical and the FE model at the peak load and when $\mathcal{E} = 20$ mm with $2\alpha_{\mathrm{m}} = 0.1$, $\phi_{\mathrm{s}} = 3$ mm and $\gamma = 0.8$ (left: FE; right: Analytical). The amplification factor is 5 for visualization purposes; (a–b) show Mode 1; (c–d) show Mode 2.



(a) Peak load (b) $\mathcal{E} = 20$ mm

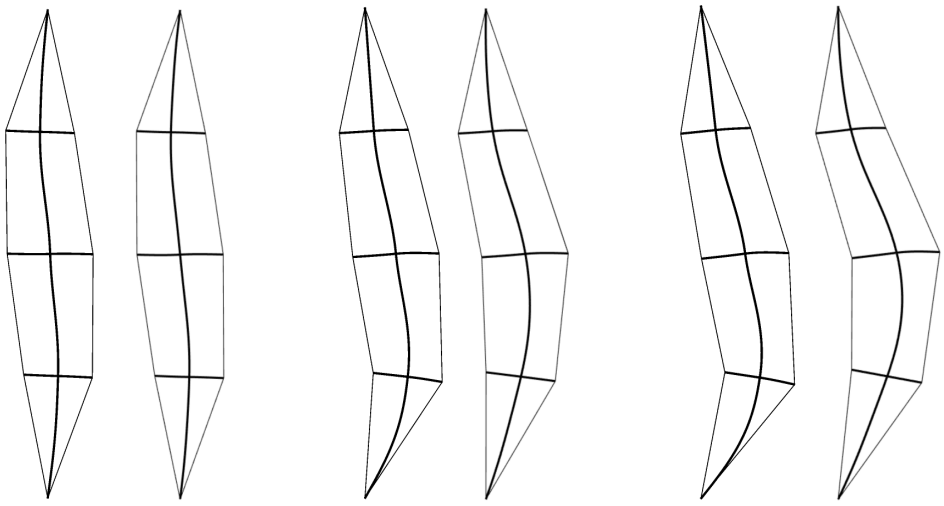
(c) Peak load (d) $\mathcal{E} = 20$ mm

Figure 23: Comparisons of post-buckling profiles between the analytical and the FE model at the peak load and when $\mathcal{E} = 20$ mm with $2\alpha_{\mathrm{m}} = 0.25$, $\phi_{\mathrm{s}} = 3$ mm and $\gamma = 0.8$ (left: FE; right: Analytical). The amplification factor is 5 for visualization purposes; (a–b) show Mode 1; (c–d) show Mode 2.



(a) Peak load (b) $\mathcal{E} = 4$ mm (c) $\mathcal{E} = 5$ mm

Figure 24: Comparisons of post-buckling profiles between the analytical and the FE model at the peak load and the interactive buckling region where $2\alpha_{\mathrm{m}} = 0.2$, $\phi_{\mathrm{s}} = 2.5$ mm and $\gamma = 0.8$ (left: FE; right: Analytical). The amplification factor is 5 for visualization purposes.



(a) Peak load (b) $\mathcal{E} = 8$ mm (c) $\mathcal{E} = 12$ mm

Figure 25: Comparisons of post-buckling profiles between the analytical and the FE model at the peak load and the interactive buckling region where $2\alpha_{\mathrm{m}} = 0.175$, $\phi_{\mathrm{s}} = 3$ mm and $\gamma = 0.8$ (left: FE; right: Analytical). The amplification factor is 5 for visualization purposes.

5. Concluding remarks

A nonlinear analytical model formulated with potential energy principles in conjunction with the Rayleigh–Ritz method has been presented. Shape functions for each part of the structure were used to derive to the total potential energy stored in the entire system. Both linear and nonlinear analyses were conducted with parametric variations. The model results clearly revealed, for the first time, the detailed process explaining how the two principal buckling modes interact when their corresponding loads are in relatively close proximity. It was also clearly identified that mode interaction in prestressed stayed columns is intimately linked to the stay slackening and crossarm bending phenomena, which were successfully modelled in the current study. Moreover, it is found that if the antisymmetric Mode 2 is marginally critical, the actual post-buckling response is dominated by nonlinear modal interactions that feature mode jumping and, to some extent, cellular buckling. Therefore there is a potential danger in overestimating the nonlinear load carrying capacity if Mode 2 is critical. The parametric ranges where interactive buckling, including mode jumping and cellular buckling, is most significant were also identified and presented for different structural configurations. It was not only demonstrated that the benchmark prestressing force T_{opt} promotes the most undesirable behaviour in terms of post-buckling instability, but also that this may be mitigated by simply increasing the initial prestressing force.

The plan for the immediate future is to develop the analytical model by introducing geometric imperfections, allowing the model to investigate more practically realistic cases. The actual optimal prestressing force in terms of the load carrying capacity and post-buckling stability will also be investigated more fully, which will allow for robust guidance on designing such components to be formulated.

References

[1] E. Belenya, Prestressed load-bearing metal structures, Moscow: Mir Publishers, 1977.

[2] R. J. Smith, J. S. Ellis, G. T. McCaffrey, Buckling of a single-crossarm stayed column, ASCE J. Struct. Div. 101 (1) (1975) 249–268.

[3] M. C. Temple, Buckling of stayed columns, ASCE J. Struct. Div. 103 (4) (1977) 839–851.

[4] K. C. Wong, M. C. Temple, Stayed column with initial imperfection, ASCE J. Struct. Div. 108 (1982) 1623–1640.

[5] E. A. Smith, Behavior of columns with pretensioned stays, ASCE J. Struct. Eng. 111 (1985) 961–972.

[6] S. L. Chan, G. P. Shu, Z.-t. Lü, Stability analysis and parametric study of pre-stressed stayed columns, Eng. Struct. 24 (2002) 115–124.

[7] M. Serra, A. Shahbazian, L. S. da Silva, L. Marques, C. Rebelo, P. C. G. da Silva Vellasco, A full scale experimental study of prestressed stayed columns, Eng. Struct. 100 (2015) 490–510.

[8] S. A. L. Andrade, P. C. G. S. Vellasco, J. G. S. Silva, Concepcao e projecto estrutural do palco principal do Rock in Rio III, Construcao Magazine 6 (2003) 4–11.

[9] S. A. L. Andrade, P. C. G. S. Vellasco, J. G. S. Silva, Sistema construtivo e montagem estrutural do palco Principal do Rock in Rio III, Construcao Magazine 7 (2003) 30–35.

[10] K. H. Chu, S. S. Berge, Analysis and design of struts with tension ties, ASCE J. Struct. Div. 89 (1963) 127–163.

[11] H. R. Mauch, Optimum design of columns supported by tension ties, ASCE J. Struct. Eng. 93 (3) (1967) 201–220.

[12] W. P. Howson, F. W. Williams, A parametric study of the initial buckling of stayed columns, Proc. Inst. Civil. Eng. 69 (1980) 261–279.

[13] H. H. Hafez, M. C. Temple, J. S. Ellis, Pretensioning of single-crossarm stayed columns, ASCE J. Struct. Div. 105 (2) (1979) 359–375.

[14] D. Saito, M. A. Wadee, Post-buckling behaviour of prestressed steel stayed columns, Eng. Struct. 30 (5) (2008) 1224–1239.

[15] D. Saito, M. A. Wadee, Buckling behaviour of prestressed steel stayed columns with imperfections and stress limitation, Eng. Struct. 31 (1) (2009) 1–15.

[16] D. Saito, M. A. Wadee, Numerical studies of interactive buckling in prestressed steel stayed columns, Eng. Struct. 31 (2) (2009) 432–443.

[17] M. A. Wadee, L. Gardner, T. A. Hunt, Buckling mode interaction in prestressed stayed columns, Proc. Inst. Civil. Eng. – Struct. Build. 166 (2013) 403–412.

[18] A. I. Osofero, M. A. Wadee, L. Gardner, Experimental study of critical and post-buckling behaviour of prestressed steel stayed columns, J. Constr. Steel Res. 79 (2012) 226–241.

[19] D. Saito, M. A. Wadee, Optimal prestressing and configuration of stayed columns, Proc. Inst. Civil. Eng. – Struct. Build. 163 (5) (2010) 343–355.

[20] M. A. Wadee, A. I. Osofero, L. Gardner, Design of prestressed stayed columns, J. Constr. Steel Res. 80 (2013) 287–298.

[21] E. J. Doedel, B. E. Oldeman, AUTO-07P: Continuation and Bifurcation Software for Ordinary Differential Equations, Concordia University, Montreal, Canada (2011).

[22] G. Augusti, Some problems in structural instability with special reference to beam of I-section, Ph.D. thesis, University of Cambridge (1964).

[23] A. H. Chilver, Coupled modes of elastic buckling, J. Mech. Phys. Solids 15 (1967) 15–28.

[24] W. J. Supple, Coupled branching configuration in the elastic buckling of symmetric structural systems, Int. J. Mech. Sci. 9 (1967) 97–112.

[25] J. M. T. Thompson, W. J. Supple, Erosion of optimum design by compound branching phenomena, J. Mech. Phys. Solids 21 (1973) 135–144.

[26] D. Orlando, P. B. Gonçalves, G. Rega, S. Lenci, Nonlinear dynamics and sensitivity to imperfections in Augusti's model, J. Mech. Mater. Struct. 6 (7–8) (2011) 1065–1078.

[27] G. W. Hunt, M. A. Peletier, A. R. Champneys, P. D. Woods, M. A. Wadee, C. J. Budd, G. J. Lord, Cellular buckling in long structures, Nonlinear Dyn. 21 (1) (2000) 3–29.

[28] C. J. Budd, G. W. Hunt, R. Kuske, Asymptotics of cellular buckling close to the Maxwell load, Proc. R. Soc. A 457 (2001) 2935–2964.

[29] M. K. Wadee, C. D. Coman, A. P. Bassom, Solitary wave interaction phenomena in a strut buckling model incorporating restabilisation, Physica D 163 (2002) 26–48.

[30] M. A. Wadee, L. Gardner, Cellular buckling from mode interaction in I-beams under uniform bending, Proc. R. Soc. A 468 (2012) 245–268.

[31] M. A. Wadee, L. Bai, Cellular buckling in I-section struts, Thin-Walled Struct 81 (2014) 89–100.

[32] M. A. Wadee, M. Farsi, Cellular buckling in stiffened plates, Proc. R. Soc. A 470 (2168) (2014) 20140094.

[33] ABAQUS, Version 6.14 Documentaion, Dassault Systèmes Simulia Corp., Providence, RI (2014).

[34] R. R. Araujo, S. A. L. Andrade, P. C. G. S. Vellasco, J. G. S. Silva, L. R. O. Lima, Experimental and numerical assessment of stayed steel columns, J. Constr. Steel Res. 64 (2008) 1020–1029.

[35] P. Li, M. A. Wadee, J. Yu, M. Wu, Stability of prestressed stayed steel columns with a three branch crossarm system, J. Constr. Steel Res. 122 (2016) 274–291.

[36] C. Zschernack, M. A. Wadee, C. Völlmecke, Nonlinear buckling of fibre-reinforced unit cells of lattice materials, Compos. Struct. 136 (2016) 217–228.

[37] M. C. Temple, M. V. Prakash, J. S. Ellis, Failure criteria for stayed columns, ASCE J. Struct. Eng. 110 (1984) 2677–2689.

[38] J. M. T. Thompson, G. W. Hunt, A general theory of elastic stability, Wiley, London, 1973.

[39] Maple, Version 2015.2, Maplesoft, a division of Waterloo Maple Inc., Waterloo, Ontario, Canada (2015).

[40] E. Riks, An incremental approach to the solution of snapping and buckling problems, Int. J. Solids Struct. 15 (1979) 529–551.

[41] N. S. Trahair, M. A. Bradford, D. A. Nethercot, L. Gardner, The behaviour and design of steel structures to EC3, 4th Edition, Taylor & Francis, London, 2008.

[42] A. I. Osofero, M. A. Wadee, L. Gardner, Numerical studies on the buckling resistance of prestressed stayed columns, Adv. Struct. Eng. 16 (2013) 487–498.

[43] J. Yu, M. A. Wadee, Numerical and analytical studies of prestressed stayed columns with multiple cross-arms, in: D. Camotim, P. B. Dinis, S. L. Chan, C. M. Wang, R. Gonçalves, N. Silverstre, C. Basaglia, A. Landesmann, R. Bebiano (Eds.), Proceedings of the eighth international conference on advances in steel structures, 2015, paper number: 186.

[44] P. R. Everall, G. W. Hunt, Mode jumping in the buckling of struts and plates: a comparative study, Int. J. Non-Linear Mech. 35 (2000) 1067–1079.

[45] J. Burke, E. Knobloch, Homoclinic snaking: Structure and stability, Chaos 17 (3) (2007) 037102.

[46] S. J. Chapman, G. Kozyreff, Exponential asymptotics of localised patterns and snaking bifurcation diagrams, Physica D 238 (2009) 319–354.

[47] BS EN10210-2, British Standard: Hot finished structural hollow sections of non-alloy and fine grain steels Part 2: Tolerances, dimensions and sectional properties, British Standards Institution (2006).